J. Appl. Comput. Mech., 11(4) (2025) 1039-1059
DOI: 10.22055/jacm.2024.47703.4770

ISSN: 2383-4536
jacm.scu.ac.ir

Shahid Chamran University of Ahvaz

Journal of Applied and Computational Mechanics

Research Paper

Analysis of External Magnetized Dissipative Thermo-convective Tangent Hyperbolic-micropolar Flow on a Rotating Non-isothermal Cone with Hall Current and Joule Dissipation: Electro-conductive Polymer Spin Coating

S. Abdul Gaffar[1], O. Anwar Bég[2], T.A. Bég[3], S. Kuharat[2], P. Ramesh Reddy[4]

[1] Mathematics and Computing Skills Unit, Preparatory Studies Center, University of Technology and Applied Sciences, Salalah, Sultanate of Oman, Email: AbdulGaffar.Shaik@utas.edu.om

[2] Multi-Physical Engineering Sciences Group, Mechanical Engineering Department, Corrosion and Coatings Lab, Room 3-08, SEE Building, University of Salford, Manchester, M54WT, UK, Email: O.A.Beg@salford.ac.uk (O.A.B.); S.Kuharat2@salford.ac.uk (S.K.)

[3] Engineering Mechanics Research, Israfil House, Dickenson Rd., Manchester, M13, UK, Email: tasveerabeg@gmail.com

[4] Department of Mathematics, Madanapalle Institute of Technology & Sciences, Madanapalle, India, Email: prreddy.mits@gmail.com

Received August 10 2024; Revised December 19 2024; Accepted for publication December 30 2024.
Corresponding author: S. Abdul Gaffar (abdulsgaffar0905@gmail.com, AbdulGaffar.Shaik@utas.edu.om)

Abstract. Motivated by spin coating operations for magnetic polymers, a theoretical and numerical study is conducted of nonlinear, steady-state boundary layer flow and heat transfer of an incompressible tangent hyperbolic non-Newtonian micropolar fluid from a spinning cone with magnetic field, viscous dissipation, Hall current, Joule dissipation and power-law variation in temperature on the cone surface. The transformed non-dimensional conservation equations are solved numerically subject to physically appropriate boundary conditions using a second-order accurate implicit finite-difference Keller Box technique. The numerical code is validated with previous studies. Increasing magnetic interaction parameter (M) accelerates the axial velocity, damps the tangential velocity and micro-rotation (near the wall) and elevates temperatures strongly. Increasing Eckert number (Ec) enhances temperature and accelerates the axial flow and damps the tangential flow and also the angular velocity (micro-rotation) near the wall, although it generates strong angular acceleration further into the boundary layer. An increment in Hall parameter (β_e) produces significant cross flow and damps the axial velocity but elevates the tangential flow and temperature (and thermal boundary layer thickness), also producing a marked acceleration in angular velocity further from the cone surface. Increasing Eringen micropolar coupling parameter K weakly reduces axial velocity near the wall but accelerates the axial flow further away. A strong acceleration in tangential flow and temperature is induced throughout the boundary layer regime with higher Eringen micropolar coupling parameter whereas. Reversal in micro-element spin (angular velocity) is suppressed near the cone surface with greater higher Eringen micropolar coupling parameter although there is a strong deceleration in the micro-rotation further towards the free stream. The simulations provide a useful insight into complex rheological magnetic spin coating operations and a solid benchmark for further computational fluid dynamics investigations.

Keywords: Non-Newtonian Tangent Hyperbolic micropolar fluid; Weissenberg number; Power-law index; Electro Conductive Polymer (ECP); Spin coating.

1. Introduction

Rotational (spin) coating involves the careful deposition of bespoke materials on revolving substrates. The centrifugal forces generated by the rotation of the body being coated can be exploited to enhance the quality of the surface finishing. The spreading coating exhibits an external boundary layer nature, and the boundary layer grows radially outwards. It is particularly popular for polymeric thin films [1]. Often spin coating is accompanied with heat transfer [2] also including forced and natural convection. Mass transfer [3] may also simultaneously be present in which case thermo-solutal (double diffusive) convection occurs. Many different geometries have been utilized for spin coating operations. At higher spin speeds, faster drying times can also be achieved relative to other coating techniques and the final coating is more uniform and consistent. The fluid dynamics of spin coating involves numerous multi-physics phenomena including non-Newtonian characteristics, electromagnetics and also curvature of the substrate. A particular advantage of coating curved surfaces is the many applications in micro-electronics, aerospace

Published online: January 06 2025

component protective coating against corrosion, metal shielding grid on the window of a fairing, curved grating in UV light protection optical elements thin-film amorphous silicon solar cells. In this regard a number of theoretical and computational studies have been communicated considering different rotating curved configurations including rotating cylinders [4], ellipsoids [5] and rotating spheres [6-8]. Another interesting geometry is the rotating cone. Anilkumar and Roy [8] used a Varga algorithm and quasi-linearization method to compute the time-dependent mixed thermo-solutal convective boundary layer flow from a vertical spinning cone in a rotating Newtonian fluid. They demonstrated that a self-similar solution is only possible when the free stream angular velocity and the angular velocity of the cone vary inversely as linear functions of time. They showed that the increasing thermal buoyancy, behaving akin to a positive pressure gradient, boosts both skin friction and Nusselt and Sherwood numbers on the cone surface and damps oscillations in the boundary layers. The effects of wall transpiration (suction and injection) on a conical body were computed by Ravindran *et al.* [9]. Tien and Tsuji [10] considered forced convection from an upright spinning cone. Many other investigations of the external boundary layer transport from a revolving cone have been communicated with diverse applications ranging from electrode coating thickness measurement in conical cathode cells for control of high-speed electrodeposition processes [11], asymptotic and Galerkin finite-element computation of thin rheological films for bell-sprayers with inertial, viscous, and surface tension effects [12], thermal control of ice accretion on jet engine rotating cone components [13], high Reynolds number boundary layers on rotating aeroengine nose cones of transonic cruise aircraft [14] and hydrocyclone chemical separation devices [15]. Mustafa [16] worked on similarity transformation of the thermal flows of the rotating cone past a stretchable disk. He observed that the centripetal/centrifugal flow properties of disk/cone are completely altered, and the flow swirling angles are increased by means of the wall deformation. Turkyilmazoglu [17] addressed the rotating flows of von Karman fluid past a stretchable/shrinkable flexible cone proving that the similar transformations reduce the deforming cone to a deforming disk. Turkyilmazoglu [18] presented the quiescent fluid swirling flows past a rotating cone using the Ackroyd's exponentially decaying series solutions. All these studies confirmed that when a significant temperature difference arises between the cone surface and the ambient fluid, there is competition between thermal buoyancy and centrifugal forces in the swirling regime.

In polymer spin coating a key characteristic is the *rheology* of the coating. Polymers exhibit a very wide range of non-Newtonian behaviours which are intimately associated with the final constitution of coatings including aesthetic quality, non-dripping properties, consistency, minimum sagging tendencies [19]. High quality polymeric coatings achieve sufficient viscosity at the application shear rate so that high build in film thickness is sustained and brush or roller drag effects are minimized. Additionally, viscoelasticity of polymers ensures that coating extensional viscosity and elasticity are balanced in order to mitigate spattering and stringing effects [20]. Many robust non-Newtonian constitutive models have been deployed to represent the complex stress-strain characteristics of polymers including thixotropic models (viscosity decreases with time), Bingham viscoplastic (yield stress behaviour), Oldroyd-B and upper convected Maxwell (viscoelasticity) [21]. All these formulations have been used successfully in non-Newtonian coating applications.

In recent years, the emergence of smart functional magnetic polymers has infiltrated coating technology. Variously known as electro-conductive polymers (ECPs) and magnetoelectric polymers (MEPs) [22] these complex materials combine the properties of polymers with magnetohydrodynamics (MHD) and ferro-hydrodynamics (FHD). They can be engineered to produce very subtle characteristics for diverse industrial applications and their simulation during spin coating requires a combination of viscous magnetofluid dynamics and rheological modelling [23]. Magnetic properties are achieved by embedding metallic conducting particles in the polymer melt which can adjust the electro-active phases of the material under the action of an external magnetic field [24]. These materials are proving to be very popular for thin film deposition. However, the presence of suspensions in these polymer matrix produces a sophisticated microstructure which cannot be accommodated with conventional non-Newtonian models, in particular when spin coating is involved since angular momentum exerts a profound effect on polymer characteristics [25]. To simulate more precisely the non-Newtonian behaviour at the microscale different approach is required. Eringen [26] pioneered the field of micro-continuum (micromorphic) fluid dynamics in the mid-1960s, wherein he provided the most robust framework to date for analysing gyratory motions of particles suspended in a viscous medium. Micropolar fluids provide a formulation in which micro-elements (finite-sized particles) can rotate independently. The micropolar theory assumes the micro-elements to be rigid, spherical and non-deformable, although the more complex Eringen micromorphic theory also includes axial deformations (stretch) of the particles [27]. Micropolar theory effectively extends the classical Navier-Stokes viscous fluid theory by including an extra angular momentum balance (micro-rotation) which features the additional degrees of freedom (gyration vector). The equations governing the flow of a micropolar fluid therefore involve a spin vector and a microinertia tensor in addition to the customary velocity vector featuring in the linear momentum-based Newtonian (Navier-Stokes) model. Micropolar fluids can support body couples, couple stresses, and a non-symmetric stress tensor. In micropolar fluids, the macroscopic velocity field is coupled with the particle rotational motion, and vortex viscosity acts as a coupling constant. The great advantage of this formulation is that the Navier-Stokes model can be extracted as a special case when gyratory motions are neglected. Micropolar theory has proved immensely effective in simulating many complex rotational flow problems ranging from electromagnetic annular nuclear duct flows [28] to rotating cone coating flows [29]. Ahmad *et al.* [30] computed finite difference solutions for hydromagnetic micropolar boundary layer convective heat and mass transfer from a rotating cone to a saturated porous medium with cross diffusion effects. They noted that higher Prandtl number suppresses temperatures whereas stronger diffuso-thermal Dufour effect enhances them. They also noted that angular velocity (Eringen micro-rotation) is reduced with stronger magnetic field and Darcy drag effects. Shamshuddin *et al.* [31] used a variational finite element code in MATLAB to visualize the 3-dimensional transient hydromagnetic micropolar coating flow on a rotating substrate with heat and mass transfer, chemical reaction, Soret and Dufour effects and radiative flux. The observed that the primary, secondary momentum, temperature and concentration fields are influenced differently with micropolar parameter, and that micro-rotation shows great sensitivity to both magnetic field and vortex viscosity. Hina *et al.* [32] used the MATLAB-based bvp4c Lobatto IIIa collocation technique to compute the steady swirling micropolar fluid from a permeable stationary disk with strong radial pressure gradient.

While the micropolar model provides an excellent insight into *microstructural* rheological characteristics (couple stresses, spin etc) it does not permit the analysis of shear thinning / thickening or visco-plasticity/elasticity in complex coating fluids. Researchers have therefore in recent years explored possible combinations of both the conventional non-Newtonian non-polar models with the micropolar model to furnish a more general formulation that can capture both gyratory motion (via the couple stress *i.e.* spin tensor) and complex shear stress-strain effects (vi the classical Cauchy tensor). These combined models include the micropolar Bingham plastic model [33] (which successfully predicts the Segre–Silberberg effect for steady flows), micropolar Buongiorno nanofluids [34], micropolar Carreau fluids [35], micropolar Eyring-Powell polymers [36], micropolar Reiner-Rivlin second grade elastic-viscous fluids [37], micropolar Reiner-Rivlin third grade elastic-viscous fluids [38] and Williamson-Maxwell viscoelastic micropolar nanofluids [39]. An alternative rheological model that has thus far not been considered in conjunction with micropolar fluids is the tangent hyperbolic (T-H) model. This model provides a constitutive equation which is valid for both low and high shear rates. It is known as a "rate-type" rheological model which includes characteristics of the relaxation time and the retardation time, both important considerations in real polymers. Furthermore, the tangent hyperbolic fluid can simulate shear-thinning (pseudoplastic) behaviour via a rheological power-law index, similar to the Ostwald-DeWaele power-law model. The T-H model has been deployed in recent years by Basha *et al.* [40] in nanofluid enrobing coating flow, Gaffar *et al.* [41] for magnetized non-isothermal coating of a cone, Malik *et al.* [42] for axisymmetric magnetic boundary layer flow on an extending horizontal pipe and Prakash *et al.* [43] for bi-axial stretching of an electroconductive polymer under the dual effects of orthogonal electrical and magnetic fields. Nasir *et al.* [44] computed the collective influence of thermal and solutal stratification on tangent hyperbolic Buongiorno nanofluid boundary layer coating flow along a porous stretching surface with thermal radiative flux, convective wall conditions and heat generation. They used the HAM (homotopic analysis method) and noted that with greater Weissenberg number velocities are reduced, temperature is enhanced with thermal Biot number and nanoparticle concentration values is depleted with solutal stratification parameter. Asogwa *et al.* [45] computed the combined influence of cross diffusion, chemical activation energy and heat source on tangent hyperbolic electro-magneto-hydrodynamic nanofluid from a stretching sheet. They showed that skin friction is suppressed with rheological power-law index increment and Nusselt number is reduced with Weissenberg number. Further studies deploying the T-H rheological model include Usman *et al.* [46] who simulated the magnetized Von Karman swirling slip convective from a radially stretching spinning disk. They observed that with stronger momentum slip at the disk surface and Weissenberg number, there is an acceleration in the radial and tangential flow whereas the opposite trends are computed with greater power-law rheological index. Reddy *et al.* [47] presented the entropy analysis of magnetohydrodynamics mixed thermal convective flows of tangent hyperbolic fluid past an isothermal wedge.

The objective of the present study is to investigate the effects of Hall current and Ohmic heating on laminar convection boundary layer flow and heat transfer in tangent hyperbolic *micropolar fluid* external to a spinning cone with power-law variation in surface temperature. Most studies of rotating micropolar or tangent hyperbolic MHD flow have neglected additional magnetic field effects such as Hall current and Ohmic heating. Both have been identified as important in real magnetic materials processing operations including coating deposition [48]. With the application of a strong magnetic field, a substantial voltage difference (or Hall voltage) is produced across an electric conductor (magnetic polymer) where the magnetic field is orthogonal to the current. The Hall current becomes significant when the magnetic field is very high or when the collision frequency is very low and mobilizes a secondary (cross) flow effect [49, 50]. Hall current MHD flows have been reported in several electromagnetic materials processing flows neglecting rotation including Shamshuddin *et al.* [51], Bég *et al.* [52] and Chandrawat *et al.* [53] (who also consider multi-phase interfacial phenomena for nuclear ducts). Mustafa [54] considered the Hall currents MHD flows past a porous rotating disk with uniform suction/blowing, viscous and Joule dissipaiton. Rotating micropolar MHD convection from a spinning cone with Hall current was previously examined by Abo-Eldahab *et al.* [55] and Dinarvand *et al.* [56], although both these investigations gave very limited interpretation of the computational results and did not include the tangent hyperbolic model. The novelty of the present study is therefore the simultaneous consideration of laminar convection boundary layer flow and heat transfer in tangent hyperbolic micropolar fluid from a rotating non-isothermal cone with Hall current, viscous dissipation and Ohmic heating (Joule dissipation) effects. As such this work generalizes for the first time all previous studies and provides to the authors' knowledge the first comprehensive assessment of this important problem of relevance to magnetic polymer spin coating operations in process mechanical engineering. A non-dimensional boundary value problem two-point is derived featuring the axial and tangential momentum equations, Eringen micro-rotation equation and heat conservation equation using boundary layer theory. A numerical solution is obtained using the implicit second-order accurate Keller box finite difference method [57]. The effects of the key control parameters, namely the Weissenberg number (We), tangent hyperbolic power law index (n), surface temperature exponent (m), Prandtl number (Pr), magnetic interaction parameter (M), Hall current (β_e), Eckert number (Ec), micropolar fluid material parameters (V, λ), Eringen coupling parameter (K) and dimensionless tangential coordinate (ξ) on tangential and axial velocities, angular velocity (micro-rotation), temperature, skin friction and heat transfer rate (local Nusselt number) characteristics are visualized graphically and in tables. Validation with earlier studies [55] is included. To the best of the authors' knowledge, the present problem has not been previously addressed in the scientific literature and constitutes an important addition to simulation in electroconductive spin coating focusing on the combined influence of microstructural, viscoelastic and shear-thinning rheology.

2. Non-Newtonian Constitutive Tangent Hyperbolic Fluid Model

The viscoelasticity and pseudoplasticity of the magnetic polymer to be investigated is studied with the tangent hyperbolic non-Newtonian model. The associated Cauchy stress tensor takes the form [40-47]:

$$\bar{\tau} = \left[\mu_\infty + (\mu_0 + \mu_\infty)\tanh\left(\Gamma\bar{\dot{\gamma}}\right)^n\right]\bar{\dot{\gamma}} \tag{1}$$

where $\bar{\tau}$ is extra stress tensor, μ_∞ is the infinite shear rate viscosity, μ_0 is the zero shear rate viscosity, Γ is the time dependent material constant, m is the rheological power law index i.e. flow behaviour index and $\bar{\dot{\gamma}}$ is defined as:

$$\bar{\dot{\gamma}} = \sqrt{\frac{1}{2}\sum_i\sum_j \bar{\dot{\gamma}}_{ij}\bar{\dot{\gamma}}_{ji}} = \sqrt{\frac{1}{2}\Pi} \tag{2}$$

Here $\Pi = tr(\mathrm{grad}V + (\mathrm{grad}V)^T)^2/2$. We consider Eq. (1), for the case when $\mu_\infty = 0$, because it is not possible to discuss the problem for the infinite shear rate viscosity and for shear thinning effects so $\Gamma\bar{\dot{\gamma}} < 1$. Then Eq. (1) takes the form:

$$\bar{\tau} = \mu_0\left[\left(\Gamma\bar{\dot{\gamma}}\right)^n\right]\bar{\dot{\gamma}} = \mu_0\left[\left(1 + \Gamma\bar{\dot{\gamma}} - 1\right)^n\right]\bar{\dot{\gamma}} = \mu_0\left[1 + n\left(\Gamma\bar{\dot{\gamma}} - 1\right)\right]\bar{\dot{\gamma}} \tag{3}$$

3. Micropolar Constitutive Model

The magnetic polymer considered in this study also exhibits a complex micro-structure. The associated balance equations for linear (translational) and angular (micro-rotation) momentum for micropolar fluids take the vectorial form [26-38]:

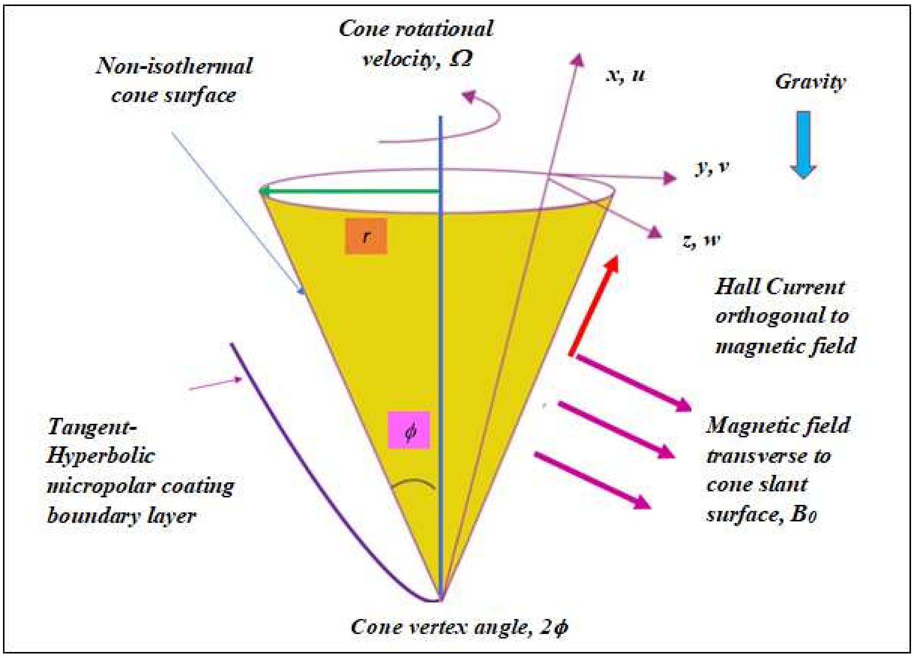

Fig. 1. Magnetic polymer spin coating on a revolving cone.

- *Conservation of Translational (Linear) Momentum*

$$(\lambda+2\mu+k)\nabla\nabla\bullet V-(\mu+k)\nabla\times\nabla\times V+k\nabla\times G-\nabla p+\rho f=\rho V' \tag{4}$$

- *Conservation of Angular Momentum (Micro-rotation)*

$$\left(\alpha^*+\beta^*+\gamma\right)\nabla\nabla\bullet h-\gamma\nabla\times\nabla\times h+k\nabla\times V-2kh+\rho l=\rho jh' \tag{5}$$

Here ( )' is a time derivative, ρ denotes the mass density of micropolar fluid, *V* is translational velocity vector, *h* is angular velocity (microrotation or gyration) vector, *f* is the body force per unit mass vector, *l* is the body couple per unit mass vector, *p* is the thermodynamic pressure, λ is the Eringen second order viscosity coefficient, *k* is the vortex viscosity coefficient, and α^*, β^* and γ arse spin gradient viscosity coefficients for micropolar fluids.

4. Magnetic Polymer Spin Coating Model

We study the steady, laminar, axisymmetric, electrically conducting, incompressible boundary layer flow of a tangent hyperbolic micropolar fluid (magnetic polymer) from a steadily spinning cone with variable wall temperature, as illustrated in Fig. 1, in an (*x*, *y*, *z*) coordinate system.

The vertical cone is rotating at a constant angular velocity around its axis of symmetry. Fluid friction, including the no-slip condition, causes a circumferential velocity, *w*, of fluid elements, which are also subjected to a centrifugal force causing the radial velocity, *v*. By virtue of mass conservation, the outward-moving fluid is being replaced by fluid eventually flowing along the cone surface with velocity *u*. An external static uniform magnetic field, B_0 acts transverse to the cone surface. The surface of the cone is held at a variable temperature proportional to the power of the distance along the cone from the vertex (*x*) i.e., $T_w(x)=T_\infty+ax^m$, where *a* and *m* are constants. The gravitational acceleration, *g*, acts downwards. The magnetic Reynolds number is assumed to be small enough to neglect magnetic induction effects since the magnetic field is not distorted. The electron-atom collision frequency is assumed to be relatively high, so that the Hall current cannot be neglected [58]. The appropriate electromagnetic equations are as follows [58]:

- *Ohm's Law for Moving Conductor with Hall Currents*

$$\mathbf{J}+\frac{\omega_e\tau_e}{B_0}(\mathbf{J}\times\mathbf{B})=\sigma[\mathbf{E}+\mathbf{q}\times\mathbf{B}] \tag{6}$$

- *Maxwell Electromagnetic Equations*

$$\vec{\nabla}\cdot\mathbf{B}=\mu_e\mathbf{J} \tag{7}$$

$$\vec{\nabla}\cdot\mathbf{E}=-\frac{\partial\mathbf{B}}{\partial t} \tag{8}$$

$$\vec{\nabla}\cdot\mathbf{J}\neq 0 \tag{9}$$

$$\vec{\nabla}\cdot\mathbf{B}=0 \tag{10}$$

Here **q** is the velocity vector $(\bar{u},\bar{v},\bar{w})$, **J** = ($J_r$, J_θ, J_z) is electrical current density vector, **B** is the magnetic field vector, **E** is the electrical field vector, ω_e, σ, τ_e are electron frequency, electrical conductivity and electron collision time respectively. Furthermore, μ_e *is the magnetic permeability* of the nanofluid. Since there exists no applied or polarization voltage on the magnetic polymer flow field, and the cone surface is electrically insulated, the electric field vector vanishes *i.e.* **E** = 0. It follows that the current density has components J_x and J_z as follows, where B_z is taken as B_0:

$$J_x = \frac{\sigma B_0^2}{(1+h^2)\rho}(\bar{u}-h\bar{v}) \tag{11}$$

$$J_z = \frac{\sigma B_0^2}{(1+h^2)\rho}(\bar{v}+h\bar{u}) \tag{12}$$

Here $h=\omega_e\tau_e$ is the dimensional Hall parameter. Under these approximations, and invoking the appropriate terms from the tangent hyperbolic model Eq. (3) and micropolar conservation equations (4) and (5), the boundary layer equations under the linear Boussinesq approximation may be written by extending the model of Abo-Eldahab and Elaziz [55]:

$$\frac{\partial(ru)}{\partial x}+\frac{\partial(rv)}{\partial y}=0 \tag{13}$$

$$u\frac{\partial u}{\partial x}+v\frac{\partial u}{\partial y}-\frac{w^2}{x}=\left(\nu+\frac{k}{\rho}\right)(1-n)\frac{\partial^2 u}{\partial y^2}+\sqrt{2}n\nu\Gamma\left(\frac{\partial u}{\partial y}\right)\frac{\partial^2 u}{\partial y^2}+g\beta(T-T_\infty)\cos\varphi+\frac{k}{\rho}\frac{\partial N}{\partial y}-\frac{\sigma B_0^2}{\rho(1+\beta_e^2)}(u+\beta_e w) \tag{14}$$

$$u\frac{\partial w}{\partial x}+v\frac{\partial w}{\partial y}+\frac{uw}{x}=\left(\nu+\frac{k}{\rho}\right)(1-n)\frac{\partial^2 w}{\partial y^2}+\sqrt{2}n\nu\Gamma\left(\frac{\partial w}{\partial y}\right)\frac{\partial^2 w}{\partial y^2}+\frac{\sigma B_0^2}{\rho(1+\beta_e^2)}(\beta_e u-w) \tag{15}$$

$$u\frac{\partial N}{\partial x}+v\frac{\partial N}{\partial y}+\frac{uN}{x}=\frac{\gamma}{\rho j}\frac{\partial^2 N}{\partial y^2}-\frac{k}{\rho j}\left(2N+\frac{\partial u}{\partial y}\right) \tag{16}$$

$$u\frac{\partial T}{\partial x}+v\frac{\partial T}{\partial y}=\alpha\frac{\partial^2 T}{\partial y^2}+\frac{\sigma B_0^2}{\rho c_p(1+\beta_e^2)}(u^2+w^2) \tag{17}$$

The corresponding boundary conditions are:

$$\begin{aligned}&\text{At } y=0,\ u=v=0,\ w=r\Omega,\ N=-\frac{1}{2}\frac{\partial u}{\partial y},\ T=T_w(x)\\&\text{As } y\to\infty,\ u\to 0,\ v\to 0,\ w\to 0,\ N\to 0,\ T\to T_\infty\end{aligned} \tag{18}$$

The dimensional stream function ψ is defined by $ru=\partial\psi/\partial y$ and $rv=-\partial\psi/\partial x$, and therefore, the continuity equation (13) is automatically satisfied. Here the *local radius* is defined as $r(x)=x\sin\varphi$.

In order to render the governing equations and the boundary conditions in dimensionless form, the following non-dimensional quantities are introduced:

$$\begin{aligned}&\xi=\frac{\zeta}{1+\zeta},\quad \eta=\frac{y}{x}\chi,\quad \psi=r\alpha\chi f,\ g(\xi,\eta)=\frac{w}{r\Omega},\quad \theta(\xi,\eta)=\frac{T-T_\infty}{T_w-T_\infty},\quad \chi=\frac{\mathrm{Re}^{1/2}}{\xi},\\&h(\xi,\eta)=\frac{\nu x^2}{\alpha^2\chi^3}N,\quad \zeta=\frac{\mathrm{Re}^{1/2}}{Ra^{1/4}},\quad \mathrm{Re}=\frac{x^2\Omega\sin\varphi}{\nu},\quad Ra=\frac{g\beta(T_w-T_\infty)x^3\cos\varphi}{\alpha\nu}\end{aligned} \tag{19}$$

In view of the transformations defined in Eq. (19), the boundary layer Eqs. (13) to (17) are reduced to the following coupled, nonlinear, *dimensionless axial and tangential linear momentum, angular momentum and energy* partial differential boundary layer equations in a (ξ,η) coordinate system emerge as:

$$\begin{aligned}&\Pr(1+K)(1-n)f'''+nW_e f''f'''+\left(2-\frac{(1-\xi)(1-m)}{4}\right)ff''-\left(1-\frac{(1-\xi)(1-m)}{2}\right)f'^2+\Pr^2\xi^4 g^2+\Pr(1-\xi)^4\theta\\&+Kh'-\frac{\Pr M\xi^2}{1+\beta_e^2}(f'+\beta_e\Pr\xi^2 g)=\xi(1-\xi)\left(\frac{1-m}{4}\right)\left(f'\frac{\partial f'}{\partial\xi}-f''\frac{\partial f}{\partial\xi}\right)\end{aligned} \tag{20}$$

$$\Pr(1+K)(1-n)g''+\Pr nW_e\xi^2 g'g''+\left(2-\frac{(1-\xi)(1-m)}{4}\right)fg'-2gf'+\frac{M}{1+\beta_e^2}(\beta_e f'-\Pr\xi^2 g)=\xi(1-\xi)\left(\frac{1-m}{4}\right)\left(f'\frac{\partial g}{\partial\xi}-g'\frac{\partial f}{\partial\xi}\right) \tag{21}$$

$$\Pr\lambda h''+\left(2-\frac{(1-\xi)(1-m)}{4}\right)fh'-\left(2-\frac{3(1-\xi)(1-m)}{4}\right)hf'-\Pr K V_1\xi^2\,(2h+\Pr f'')=\xi(1-\xi)\left(\frac{1-m}{4}\right)\left(f'\frac{\partial h}{\partial\xi}-h'\frac{\partial f}{\partial\xi}\right) \tag{22}$$

$$\theta''+\left(2-\frac{(1-\xi)(1-m)}{4}\right)f\theta'-mf'\theta+\frac{Ec M}{1+\beta_e^2}(f'^2+\Pr^2\xi^4 g^2)=\xi(1-\xi)\left(\frac{1-m}{4}\right)\left(f'\frac{\partial\theta}{\partial\xi}-\theta'\frac{\partial f}{\partial\xi}\right) \tag{23}$$

The transformed dimensionless wall and free stream boundary conditions (18) assume the form:

$$\begin{aligned}&\text{At}\quad \eta=0,\quad f=0,\quad f'=0,\quad g=1,\quad h=-\frac{\Pr}{2}f'',\quad \theta=1\\&\text{As}\quad \eta\to\infty,\quad f'\to 0,\quad g\to 0,\quad h\to 0,\quad \theta\to 0\end{aligned}\tag{24}$$

Here primes denote the differentiation with respect to η, $\Pr=\nu/\alpha$, $W_e=\sqrt{2}\,\nu\Gamma\chi^3/x^2$, $M=\sigma B_0^2/\rho\Omega\sin\varphi$, $Ec=\alpha\chi^2\Omega\sin\varphi/c_p(T_w-T_\infty)$, $K=k/\mu$, $\lambda=\gamma/j\mu$, and $V_1=\nu/j\Omega\sin\varphi$. All these parameters are defined in the notation section. The skin-friction coefficient components in the axial and tangential directions (shear stresses at the cone surface), Eringen wall couple stress and Nusselt number (heat transfer rate) can be defined using the transformations (19) and yield the following expressions:

$$\tau_{wx}=(1+K)(1-n)f''(\xi,0)+\frac{n}{2\Pr}W_e\left(f''(\xi,0)\right)^2+\frac{K}{\Pr}h\tag{25}$$

$$\tau_{wz}=(1+K)(1-n)\Pr\xi^2 g'(\xi,0)+\frac{\Pr n}{2}W_e\xi^4\left(g'(\xi,0)\right)^2\tag{26}$$

$$\mathrm{Wcs}=\Pr\left(1+\frac{K}{2}\right)h'\tag{27}$$

$$Nu=-\theta'(\xi,0)\tag{28}$$

The location, $\xi\sim 0$, corresponds to the vicinity of the *lower stagnation point* on the cone. For this scenario, the model defined by Eqs. (20) to (23) contracts to an ordinary differential boundary value problem:

$$\Pr(1+K)(1-n)f'''+nW_e f''f'''+\left(2-\frac{1-m}{4}\right)f f''-\left(1-\frac{1-m}{2}\right)f'^2+\Pr\theta+Kh'=0\tag{29}$$

$$\Pr(1+K)(1-n)g''+\left(2-\frac{1-m}{4}\right)fg'-2gf'+\frac{M}{1+\beta_e^2}(\beta_e f')=0\tag{30}$$

$$\Pr\lambda h''+\left(2-\frac{1-m}{4}\right)fh'-\left(2-\frac{3(1-m)}{4}\right)hf'=0\tag{31}$$

$$\theta''+\left(2-\frac{1-m}{4}\right)f\theta'-mf'\theta+\frac{EcM}{1+\beta_e^2}\left(f'^2\right)=0\tag{32}$$

5. Numerical Solution with Keller Box Method and Validation

The general model defined by Eqs. (20) to (24) is solved using the unconditionally stable implicit finite difference technique introduced by Keller [57]. The Keller-box finite difference method (KBFDM) has a second order accuracy with arbitrary spacing and attractive extrapolation features. In the MATLAB symbolic software environment, this numerical technique is coded to solve the nonlinear boundary value problem defined by Eqs. (20) to (24) with boundary conditions (25). This technique, despite recent developments in other numerical methods, remains a powerful and very accurate approach for boundary layer flow equation systems which are generally parabolic in nature. It is unconditionally stable and achieves exceptional accuracy. It also has the advantage that partial differential equation systems in two or more space variables and also time variable can be solved very easily. Magnetohydrodynamics applications of KBFDM are reviewed in Bég [58]. This method has also been applied successfully in many rheological flow problems in recent years. These include Jeffrey viscoelastic flows [59], shear thinning convective flows from curved bodies with entropy generation minimization [60], non-Newtonian nanofluid transport in tilted ducts [61], micropolar convection from a curved substrate [62], Falkner-Skan wedge coating flow of magnetic tangent hyperbolic polymer flows with wall slip [63, 64] and Hall current porous media MHD generator transport [65]. The Keller-Box discretization is fully coupled at each step which reflects the physics of parabolic systems – which are also fully coupled. Discrete calculus associated with the Keller-Box scheme has also been shown to be fundamentally different from all other physics capturing numerical methods, as elaborated by Keller [57]. The Keller Box Scheme comprises four stages.

1. Decomposition of the N^{th} order partial differential equation system to N first order equations.
2. Finite Difference Discretization.
3. Quasi-linearization of Non-Linear Keller Algebraic Equations and finally.
4. Block-tridiagonal Elimination solution of the Linearized Keller Algebraic Equations.

The methodology is summarized as per the MATLAB-based in-house code along with a representative Keller box (cell) and boundary layer grid design in Fig. 2.

The 9^{th} order coupled system defined by Eqs. (20) to (23) is reduced to 9 first order differential equations via suitable variable substitutions. The code runs in several minutes on a laptop or desktop PC and excellent convergence is achieved. To validate the KBFDM code, a benchmark comparison has been made with the earlier numerical solutions of Eldahab and Elaziz [55], in the absence of tangent hyperbolic parameters i. e. n = 0, We = 0. Table 1 documents the KBFDM results for Nusselt number, $Nu=-\theta'(\xi,0)$, with those in [55] for various values of magnetic interaction parameter M, Hall parameter β_e and Eckert number Ec, both at the vertex point *i.e.* boundary layer leading edge $(\xi=0)$ and also further along the slant surface from the cone vertex $(\xi=1)$. The solutions are found to be in excellent agreement. Confidence in the accuracy of the KBFDM code is therefore clearly confirmed.

Table 1. Comparison values of $-\theta'(\xi,0)$ for various values of M, β_e and Ec when $\lambda = K = 0.5$, $m = 2$, $\Pr = 1$ and $V = 0.1$.

M	β_e	Ec	$\xi = 0$		$\xi = 1$	
			Eldahab and Elaziz [55]	KBFDM	Eldahab and Elaziz [55]	KBFDM
0.0			0.69338	0.69335	0.62986	0.62984
0.5	0.2		0.68652	0.68650	0.34940	0.34934
1.0		0.5	0.67934	0.67931	0.12904	0.12901
	0.2		0.67934	0.67931	0.12904	0.12901
	1.0		0.68624	0.68621	0.45938	0.45932
	1.5		0.68903	0.68900	0.55746	0.55741
1.0		0.0	0.69338	0.69335	0.47751	0.47749
	0.2	0.5	0.67934	0.67931	0.12904	0.12901
		1.0	0.66394	0.66391	-0.24731	-0.24729

6. Numerical Results and Interpretation

Comprehensive solutions have been obtained and are presented in Figs. 2 to 26 and Tables 2 and 3. The numerical problem comprises two independent space variables (ξ,η), four dependent fluid dynamic variables (f, g, h, θ), and eleven thermo-physical and body force control parameters, namely, We, n, m, M, Pr, Ec, V, λ, β_e, K, ξ. The following default parameter values i.e. $We = n = 0.3$, $Pr = 7$, $m = 1$, $K = 3$, $M = \beta_e = \lambda = Ec = 0.5$, $V = 0.2$, $\xi = 1.0$ are prescribed (unless otherwise stated). Aqueous-based magnetic polymers are studied. All data is extracted to represent physically realistic scenarios [55]. For the primary shear stress (C_{fx}), secondary shear stress (C_{gx}), wall couple stress (Wcs) and Nusselt number (Nux) plots, the variation with stream-wise coordinate is considered.

Figures 3 to 6 depicts the effects of power law index n on the axial velocity (f'), tangential velocity (g), angular velocity (h) and temperature (θ) distributions through the boundary layer regime. Figure 3 shows the impact of power-law rheological index on axial velocity evolution with transverse coordinate (η). This parameter features in the modified shear terms, $\Pr(1+K)(1-n)f'''$, $+nW_e f'' f'''$, in the axial momentum Eq. (20). When $n = 0$ the tangent hyperbolic effect is negated and the first term contracts to the *purely micropolar case* and the latter term vanishes. Note that the case of a Newtonian fluid is only retrieved when both $n = K = 0$. As n is increased the pseudoplasticity of the fluid is increased and viscosity is curtailed. This induces a strong decrease in the axial velocity magnitudes closer to the cone surface. However, after a critical point in the boundary layer is reached $\eta \sim 4$, the stress relaxation allows an acceleration effect which is sustained into the free stream. The rheological shear-thinning characteristic therefore has a complex influence on axial velocity distribution. Entanglement of the magnetic polymer chains also contributes to the modification in viscosity [19, 21]. The dominant effect is flowing acceleration which implies a reduction in momentum (hydrodynamic) boundary layer thickness. There is also a spiralling effect induced in the boundary layer structure due to rotation wherein the axial and tangential boundary layer growth interacts. However, to visualize this a fully 3-dimensional simulation is required which is not considered here but may be explored via a commercial CFD software such as ANSYS FLUENT in the future.

Figure 4 illustrates that a consistent depletion in tangential velocity is induced with an increment in rheological power law index, n. This tangential flow deceleration manifests in a reduction in a thicker tangential momentum boundary layer. As with the axial momentum, the shear terms in Eq. (21), viz, $\Pr(1+K)(1-n)g''$, $\Pr nW_e\xi^2 g' g''$ are also strongly influenced by power-law index, n. Since linear momentum is conserved in the rotating regime, the boost in axial momentum is compensated for by a reduction in tangential momentum, especially at lower rotating speeds of the cone, as considered here. No tangential flow reversal is computed *i.e.*, g values are consistently positive at all values of transverse coordinate. The coating thickness and boundary layer structure can therefore be successfully manipulated via the deployment of different shear-thinning polymers [21, 50].

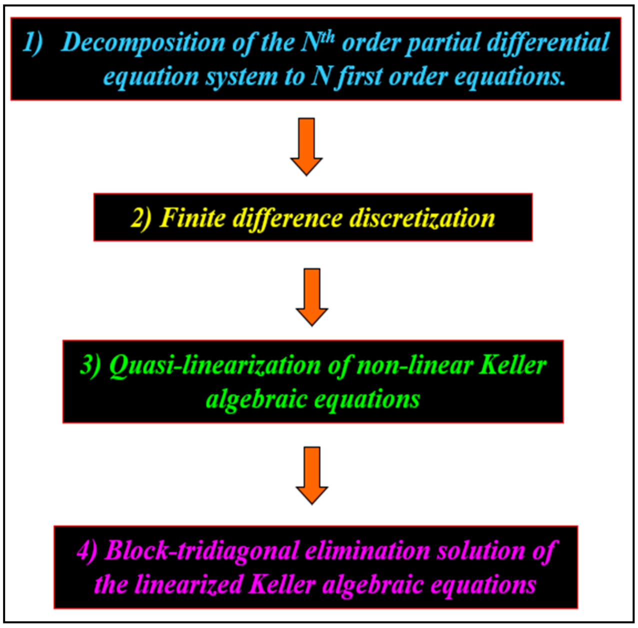

Fig. 2. Stages involved in the Keller box implicit finite difference scheme.

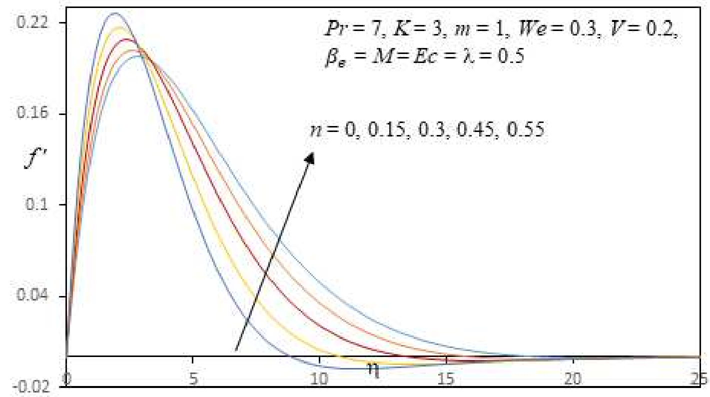

Fig. 3. Influence of n on axial velocity profiles.

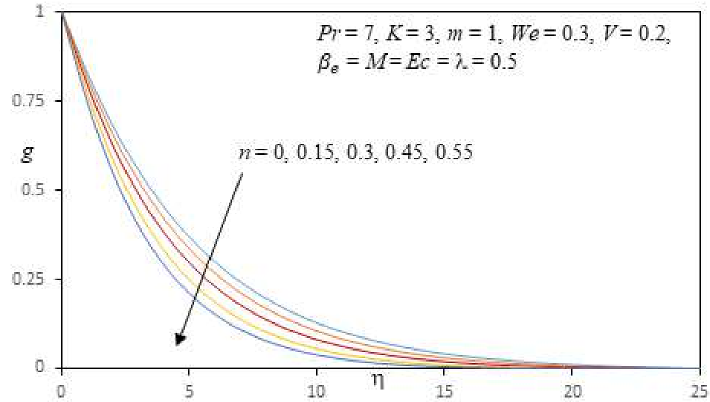

Fig. 4. Influence of n on tangential velocity profiles.

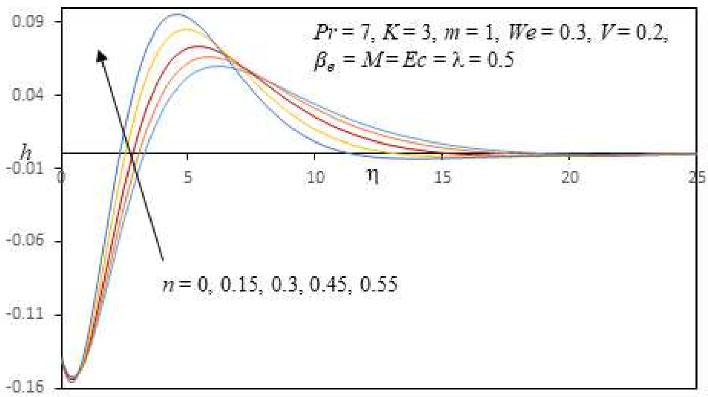

Fig. 5. Influence of n on angular velocity profiles.

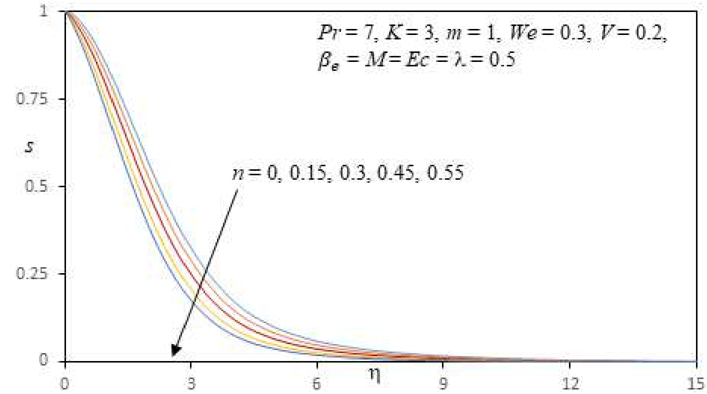

Fig. 6. Influence of n on temperature profiles.

In both the axial and tangential velocity distributions, asymptotically smooth convergence is achieved in the free stream testifying to the prescription of an adequately large infinity boundary condition in the KBFDM code. It is also noteworthy that the coating thickness in fact changes with time as a function of the substrate geometry (cone), the rotation rate, the rheological properties of the coating liquid, and the time-dependent distribution of the coating liquid. In the present study we have confined attention to steady state rotation and therefore do not explicitly address transient effects. These will be considered in a future study.

Figure 5 depicts the response in Eringen micro-rotation (angular velocity) over the same range of rheological power-law index values (0 to 0.55). A much more complex distribution is computed with oscillatory topology. The micro-element gyratory motions are initially weakly suppressed very close to the cone surface with higher n and in fact spin is reversed strongly (negative h values). However, micro-elements are subsequently accelerated strongly in the same direction of rotation as the cone itself (positive h values). This is sustained for some distance into the boundary layer transverse to the wall. Thereafter a deceleration in angular velocity is observed, although reverse spin is not computed and micro-rotation vanishes in the free stream (edge of the boundary layer). The tangent hyperbolic power-law rheological index does not explicitly arise in the angular momentum Eq. (22). However, there is very strong coupling between the angular momentum and both linear momentum fields via the terms, $\Pr(1+K)(1-n)f'''$ and in particular the term, Kh' in Eq. (20), the term $\Pr(1+K)(1-n)g''$ in Eq. (21) and the convective terms, $(2-(1-\xi)(1-m)/4)fh'$, $-(2-3(1-\xi)(1-m)/4)hf'$, $-\Pr KV_1\xi^2(2h+\Pr f'')$ and $f'\partial h/\partial\xi - h'\partial f/\partial\xi$ in the micro-rotation Eq. (22). The power-law shear-thinning effect is therefore indirectly experienced in the angular momentum Eq. (22). The variation in the behaviour is also connected to the inhibition of microelements to sustain rotary motions near the boundary which produces strong retardation. Further from the wall the space available is much greater and stronger co-rotation with the spinning cone is therefore possible. It would therefore appear that strongly pseudoplastic magnetic polymers (n = 0.55) encourage gyration motions at intermediate distances from the spinning cone surface whereas they oppose these motions towards the periphery of the boundary layer. This is also intimately connected with the micro-rotation boundary condition prescribed at the wall, viz at $\eta=0,\ g=1,\ h=-\Pr f''/2$ in Eq. (24). As noted by Peddieson [66], the wall boundary condition on h assumes that the micro-rotation vector is directly related to shear stress with micro-gyration parameter (boundary parameter). The case selected corresponds to that in which the anti-symmetric component of the stress tensor is eliminated at the surface and physically this means that there is a weak (dilute) concentration of micro-elements, which is the most practical approach available for simulations. For this scenario micro-structure effects near the solid boundary become negligible, and the rotation is only due to fluid shear, and therefore angular velocity and gyration vector are identical in the regime as noted by Gorla and Takhar [67].

Figure 6 reveals that temperature is significantly suppressed with higher n values. Smooth monotonic decays are observed and converge after some distance into the boundary layer. Thermal boundary layer thickness is therefore also depleted with greater pseudoplasticity of the magnetic polymer. Of course, as with the micro-rotation distribution, the rheological parameter n does not arise explicitly in the energy Eq. (23). However, the multiple coupling terms in this equation, namely, $(2-(1-\xi)(1-m)/4)f\theta'$, $-m\theta f'$ and $f'\partial\theta/\partial\xi-\theta'\partial f/\partial\xi$ link the temperature field strongly to the axial momentum Eq. (20). The thermal diffusion is therefore influenced by the modification in axial velocity which in turn is adjusted by the viscosity modification via the tangent hyperbolic index (n). In the absence of pseudoplasticity (shear-thinning), n = 0 and maximum temperatures are computed and vice versa for n = 0.55 (minimum temperatures). The implication is that neglection of the shear thinning rheological behaviour leads to a distinct over-prediction in temperature *i.e.* suggests strong heating, whereas actual magnetic polymers are subjected to cooling due to the shear thinning effect, as noted in [21].

Figures 7 to 10 illustrates the effect of the magnetic interaction parameter M, on the axial velocity (f'), tangential velocity (g), angular velocity (h) and temperature (θ), distributions through the boundary layer regime. The parameter $M=\sigma B_0^2/\rho\Omega\sin\varphi$ and is also known as the rotational Stuart number. It embodies the relative contribution of Lorentzian electromagnetic force and the rotational inertial force in the regime. It features in the term, $-\Pr M\xi^2(f'+\beta_e\Pr\xi^2 g)/(1+\beta_e^2)$. only in the axial momentum Eq. (20) and is also present in the tangential Eq. (21), in the term, $M(\beta_e f'-\Pr\xi^2 g)/1+\beta_e^2$. When M = 0 magnetic field effects vanish, and the polymer becomes electrically non-conducting. In linear channel (duct) MHD flows the influence of M is always to damp the velocity field. However, in rotational flows, due to the different velocity fields (axial, tangential), the magnetic force exerts a more complex influence. Figure 7 shows that stronger magnetic field accelerates the axial flow strongly and maximum axial velocity corresponds to the maximum magnetic field intensity, viz M = 1 for which both Lorentzian and inertial forces are exactly balanced. Peak velocity arises close to the cone surface but is progressively displaced further into the boundary layer transverse to the cone surface (wall) with increment in M.

Figure 8 indicates that tangential velocity is strongly damped with increment in M. Unlike the axial distribution, the tangential field again exhibits a monotonic decay from the cone surface to the free stream i.e. there is no peak velocity computed near the wall. The maximum velocity always arises at the wall. A very weak axial flow reversal (negative velocities) is computed further towards the free stream. This pattern has also been computed by Eldahab and Elaziz [55] and Dinarvand *et al.* [56], although in neither of these studies is any physical explanation provided. Two Lorentzian magnetic force components (axial and tangential) are generated by the static and uniform magnetic field applied in the radial direction and which is mutually orthogonal to both the axial and *tangential directions.*

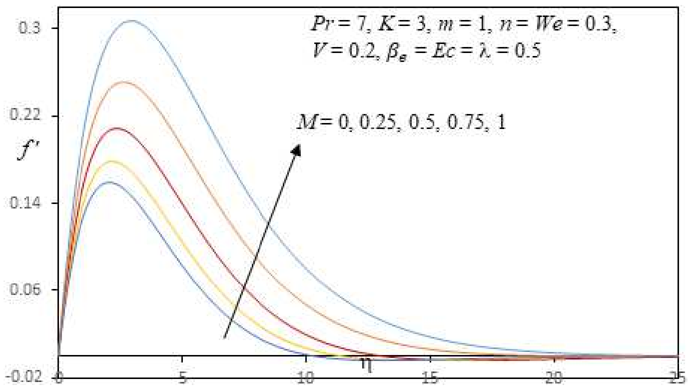

Fig. 7. Influence of M on axial velocity profiles.

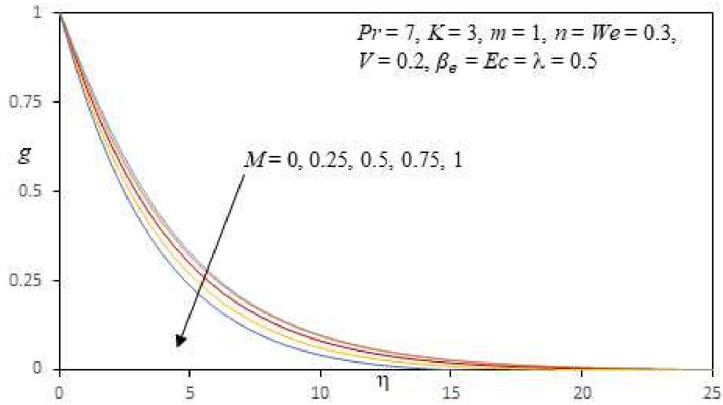

Fig. 8. Influence of *M* on tangential velocity profiles.

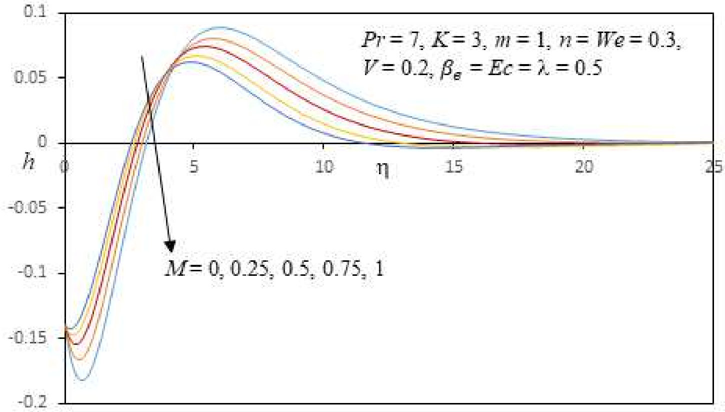

Fig. 9. Influence of *M* on angular velocity profiles.

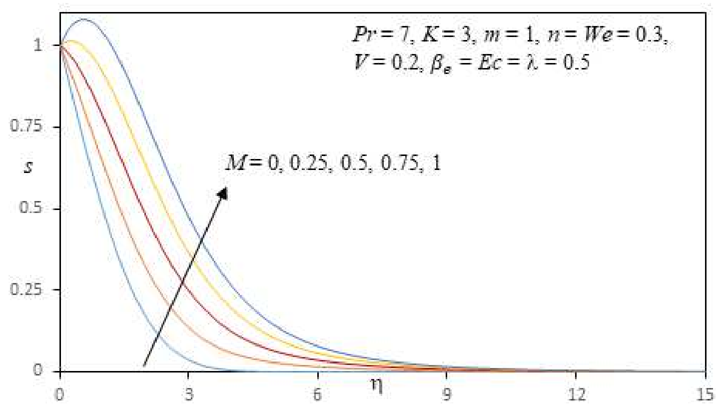

Fig. 10. Influence of *M* on temperature profiles.

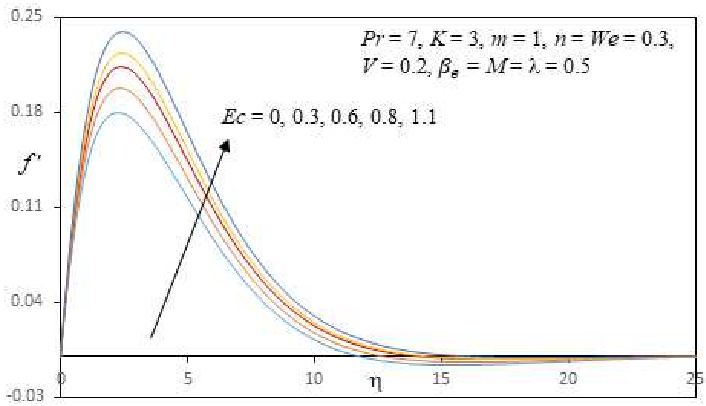

Fig. 11. Influence of *Ec* on axial velocity profiles.

The destruction in tangential momentum is compensated for by a boost in axial momentum which is required for enforcing momentum conservation in the regime. For the tangential field, therefore maximum velocity arises for the non-magnetic scenario (M = 0) and minimal velocity for the strongly magnetic case (M = 1) which is the opposite for the axial field. Coating designers can therefore control both the tangential velocity field and axial field with this magnetic field configuration but to different outcomes. However, the non-intrusive nature of an external magnetic field clearly does offer substantial benefits since it is very cost effective and indeed the orientation of the magnetic field can be modified to influence the velocity fields in a desired fashion. This facility is proving very popular in modern spin coating with magnetic materials and also reduces the wastage in bulk coating liquids required [68].

Figure 9 shows that near the cone surface a considerable reduction in angular velocity is computed with increment in magnetic interaction parameter, M. In the approximate range $0<\eta<3$, reverse spin is present *i.e.* the micro-elements rotate in the opposite direction to the cone rotation. Beyond this point generally co-rotation of micro-elements and the cone is observed, although only after the critical location of $\eta\sim 4$, *does the influence of magnetic field later*. There is a progressive boost in micro-rotation starting at this point int the boundary layer which is sustained to the free stream. As M is increased the peak micro-rotation is also enhanced and migrates further from the wall. Again, asymptotically smooth profiles are achieved in the free stream where gyratory motions vanish.

Figure 10 shows that temperature is prominently elevated with an increase in magnetic interaction parameter, M. For M < 1 no temperature overshoot is computed near the wall since the inertial rotational force dominates the Lorentz electromagnetic force. For M = 1 the overshoot is computed. The rotating magnetic polymer has to drag itself against the action of the radial magnetic field. This supplementary work expended is dissipated as thermal energy which heats the magnetic polymer. The resistance to electrical current by the magnetic polymer produces a different type of dissipation known as Joule heating (Ohmic dissipation) which is considered next. Effectively the ramp up in magnetic field intensity produces a thickening in the thermal boundary layer on the cone surface.

Figures 11 to 14 illustrates the effect of the Eckert number Ec, on the axial velocity (f'), tangential velocity (g), angular velocity (h) and temperature (θ) distributions with transverse coordinate (η). This parameter features in the coupled viscous heating and Ohmic heating terms, $EcM(f'^2+\Pr^2\xi^4 g^2)/(1+\beta_e^2)$ in the energy Eq. (23). Evidently both axial and tangential velocity fields are influenced by this parameter. Ec physically represents the relative contribution of kinetic energy expended as internal friction to the boundary layer enthalpy difference. It arises both in high speed and low velocity transport and is generated by molecular ballistic collisions in the magnetic polymer due to internal friction which create a heating effect. While the axial flow is accelerated (Fig. 11) the tangential flow is however decelerated.

Maximum axial velocity arises for Ec = 1.1 whereas the maximum tangential velocity (Fig. 12) is computed for Ec = 0 (absence of viscous and Ohmic heating). The strong coupling between the axial and tangential momentum and the angular momentum Eq. (22) also manifests in a significant modification in micro-rotation in Fig. 13. Initially the micro-rotation is negative (reverse spin) near the cone surface and is suppressed with Eckert number increment. However further from the wall the angular velocity is elevated strongly indicating that the dissipation in mechanical energy is encouraging to gyratory motions. Angular momentum boundary layer thickness is therefore accentuated with greater viscous heating. The overall kinetic energy in the tangential flow is reduced, and this is converted to thermal energy.

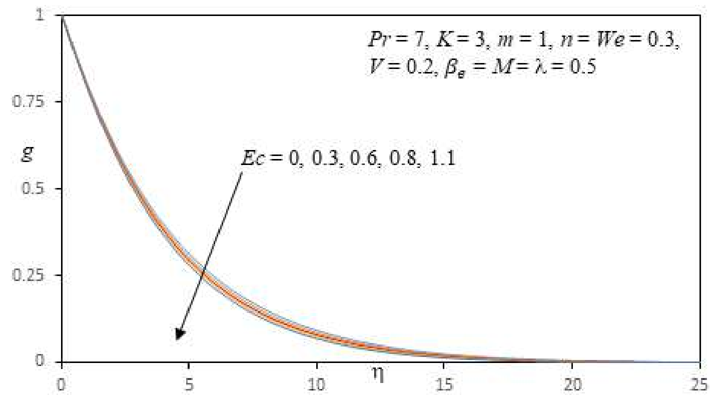

Fig. 12. Influence of Ec on tangential velocity profiles.

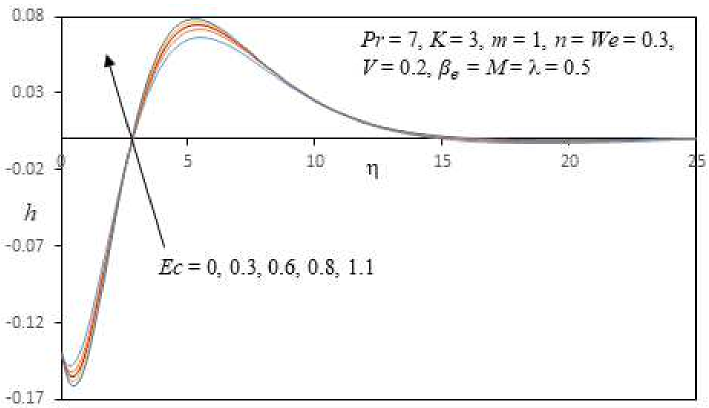

Fig. 13. Influence of Ec on angular velocity profiles.

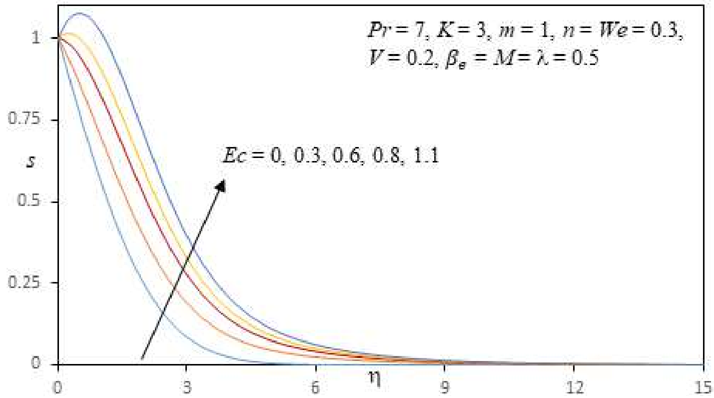

Fig. 14. Influence of Ec on temperature profiles.

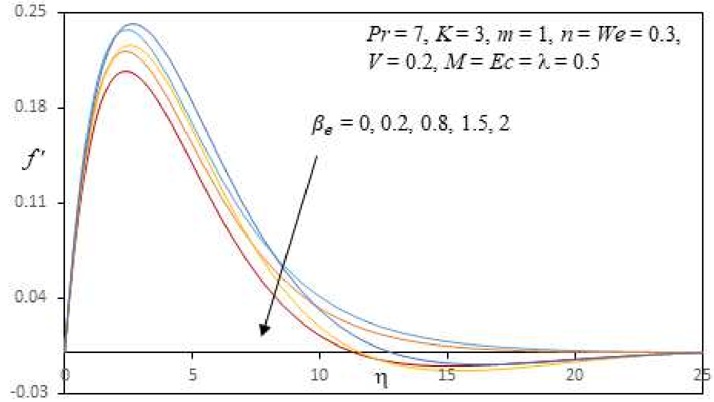

Fig. 15. Influence of β_e on axial velocity profiles.

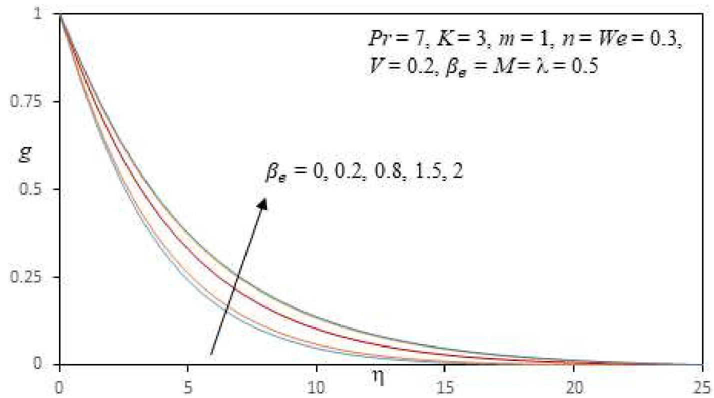

Fig. 16. Influence of β_e on tangential velocity profiles.

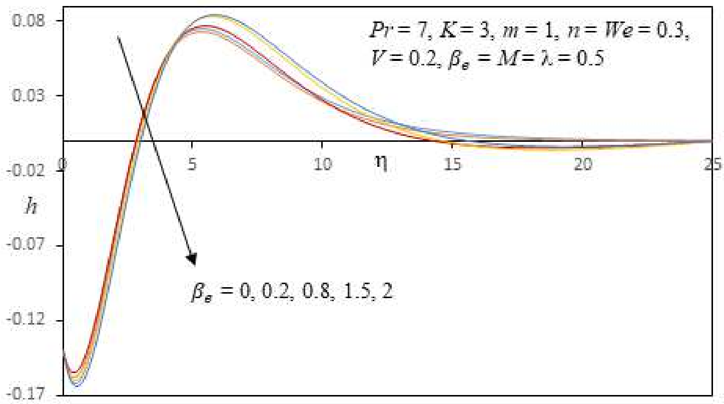

Fig. 17. Influence of β_e on angular velocity profiles.

As a result, a *strong heating effect* is produced (Fig. 14) and temperatures are boosted. Thermal boundary layer thickness is greatly boosted with Eckert number. Again, the temperature overshoot is computed in Fig. 14 but only for Ec = 1.1 but is absent for smaller values of this parameter. The neglection of viscous heating (Ec = 0) is therefore not advisable in polymeric coating dynamic simulations. Viscous heating is known to be a significant consideration in polymer spin coating manufacturing and should be included [22].

Figures 15 to 18 illustrates the effect of the Hall current β_e, on the axial velocity (f'), tangential velocity (g), angular velocity (h) and temperature (θ) distributions through the boundary layer regime. This parameter features in $-\Pr M\xi^2(f'+\beta_e \Pr \xi^2 g)/(1+\beta_e^2)$ in the axial momentum Eq. (20), $M(\beta_e f' - \Pr \xi^2 g)/(1+\beta_e^2)$ in the tangential momentum Eq. (21) and $Ec M(f'^2 + \Pr^2 \xi^4 g^2)/(1+\beta_e^2)$ in the energy Eq. (23). It always arises as an inverse squared term and is responsible for the crossflow nature. The Hall parameter is also coupled with the magnetic interaction parameter, M. The Hall current effect quantifies the charge separation phenomenon in a conductive medium (*i.e.* the magnetic polymer) moving in a magnetic field. This charge separation is produced by the opposing Lorentz forces on the positive and negative charges, and leads to an externally measurable voltage, termed the Hall voltage, as noted in Hughes and Young [69]. The Hall voltage amplitude is controlled effectively by the strength of the Lorentz force and the charge density and mobility. It can be significant in spin coating operations as noted by Inudo *et al.* [68]. Hall voltage is directly proportional to the product of electrical conductivity and axial magnetic field. The case of $\beta_e \to 0$ corresponds to vanishing Hall current. Figure 15 shows that a strong damping effect is induced in the axial velocity field with growth in the Hall parameter.

However, a significant acceleration is induced in the tangential flow (Fig. 16) over the same change in Hall current parameter values. The re-distribution in linear momentum is responsible for the different responses in the velocity components. Furthermore, the polarity of the Hall terms is different in both Eqs. (20) and (21). It is negative in the former and positive in the latter. This results in an axial velocity enhancement and tangential velocity decrement with modification in β_e. The interplay between both linear velocity components is also exacerbated by the crossflow effect. This behavior has also been computed in [55] although it was not elaborated on to any great length. The momentum diffusion in the spin coating regime can therefore be controlled via the Hall effect in addition to the radial magnetic field, providing designers with a dual strategy for flow control in the swirling regime. It is noteworthy that ion slip has been neglected in the current simulations since it requires significantly larger magnetic field strengths than those considered here as noted in [52].

Figure 17 demonstrates that initially the micro-rotation is significantly impeded in the boundary layer in close proximity to the cone surface with higher Hall current parameter values; further from the boundary there is however a switch in the effect and considerable acceleration in the angular momentum is produced, although near the free stream a spin reversal is again computed. The micro-rotation field exhibits a more complex interplay with both magnetic field and Hall current compared with the axial and tangential momenta fields. The magnetic particles in the polymer coating are affected very differently and this "polar" behavior cannot be captured with the conventional family of rheological models.

Temperature is greatly enhanced with increment in Hall parameter (Fig. 18). Vanishing Hall current therefore results in a cooling in the coating regime. Strong Hall current encourages thermal conduction from the wall (cone surface) to the bulk fluid and boosts thermal boundary layer thickness. While this response is maintained at all locations transverse to the cone surface it is most prominent at intermediate distances from the wall. This pattern of temperature topologies has also been noted in many other studies, whether Newtonian or non-Newtonian including Abo-Eldahab and Elaziz [55]. The inclusion of Hall current effects is strongly justified in more elegant simulations of magnetic polymer spin coating. It exerts a tangible influence on all the flow characteristics and also influences asymptotic behaviour in the far field.

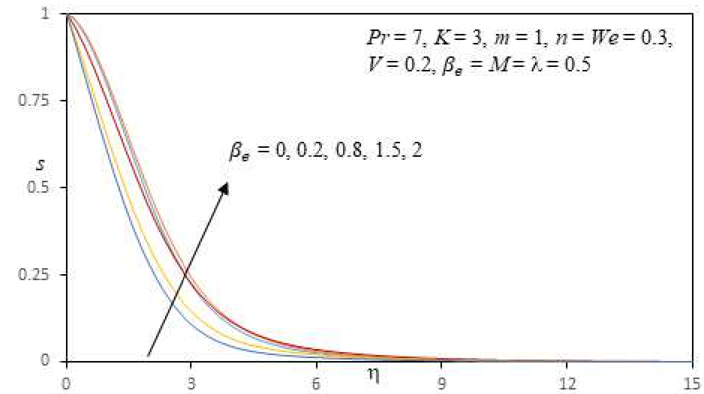

Fig. 18. Influence of β_e on temperature profiles.

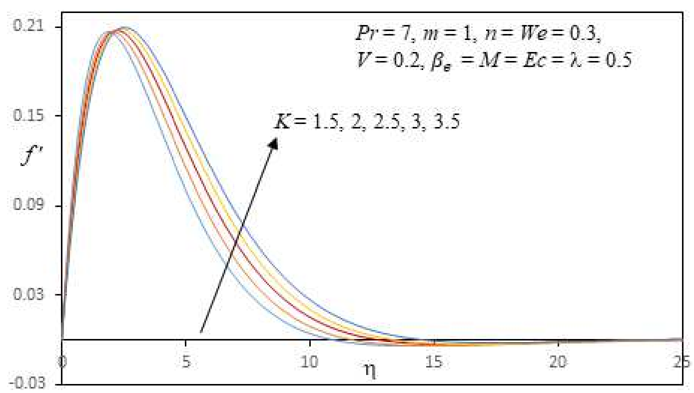

Fig. 19. Influence of K on axial velocity profiles.

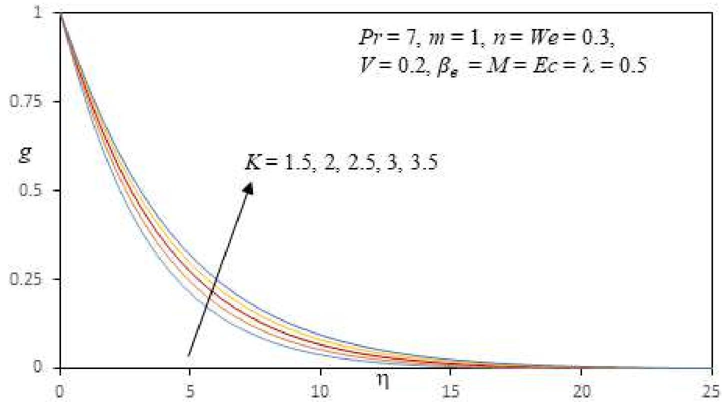

Fig. 20. Influence of K on tangential velocity profiles.

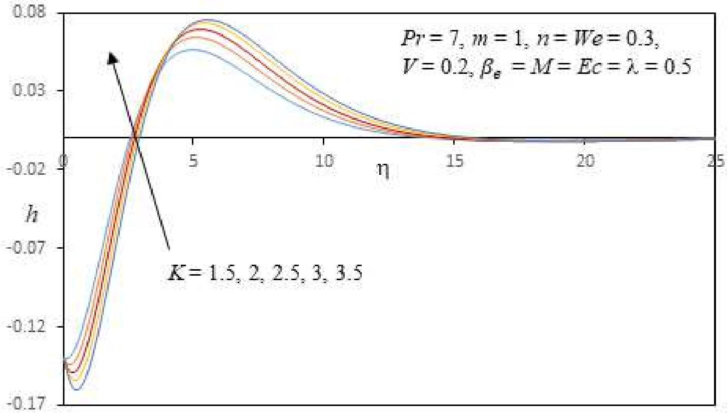

Fig. 21. Influence of K on angular velocity profiles.

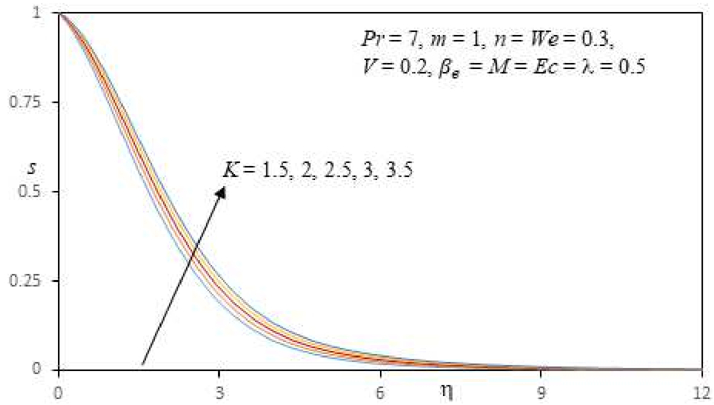

Fig. 22. Influence of K on temperature profiles.

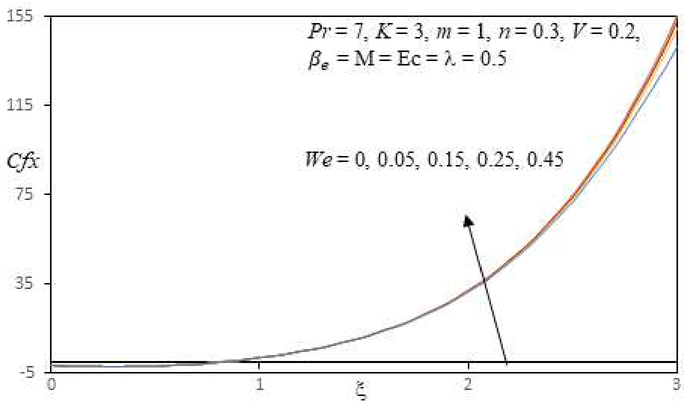

Fig. 23. Influence of We on primary shear stress profiles.

Figures 19 to 22 illustrates the effect of the Eringen micropolar coupling parameter K, on the axial velocity (f'), tangential velocity (g), angular velocity (h) and temperature (θ) distributions through the boundary layer regime. $K = k/\mu$ expresses the relative role of Eringen vortex viscosity to Newtonian dynamic viscosity. When K vanishes gyratory motions of micro-elements are negated, and the tangent hyperbolic behaviour alone is retained. This parameter, also known as Eringen number [70] is isolated to the modified axial shear term, $\Pr(1+K)(1-n)f'''$ in Eq. (20) and the modified tangential shear term, $\Pr(1+K)(1-n)g''$ in Eq. (21). In the vicinity of the cone surface a weak deceleration in axial velocity (Fig. 19) is induced with increment in K although no flow reversal is observed. Further into the boundary layer however a significant elevation is produced with larger K values. As K is increased the intensity of axial flow is boosted and a strong elevation in axial momentum boundary layer thickness is generated.

Similarly in Fig. 20, a considerable elevation in tangential velocity is produced with Eringen number, K. As in other plots the tangential profiles consistently decay from the wall with transverse coordinate, η. Clearly stronger micropolarity (K) encourages momentum diffusion in both the axial and tangential velocity fields and this confirms the excellent drag-reducing properties of micropolar fluids [32-36].

Increasing Eringen number exerts a more sophisticated influence on the microrotation field (Fig. 21). It features in the term, $-\Pr K V_1 \xi^2 (2h + \Pr f'')$ in Eq. (22), which is strongly influenced also by the axial velocity field and also the streamwise coordinate, ξ. Close to the cone surface $(\eta = 0)$ the reverse spin is systematically reduced with greater K values. Further from the wall however, although peak micro-rotation arises around $\eta \sim 5$, *there is an inhibition in micro-rotation development and deceleration in gyratory motions, although no reverse spin is observed*. The micro-rotation peak is displaced closer to the cone surface also with greater K values.

Temperature (Fig. 22) experiences a considerable boost with a hike in K values. Therefore, heating in the spinning boundary layer regime is produced with stronger micropolar fluids. Thermal boundary layer thickness is significantly boosted in the magnetic polymer with higher K values.

Figures 23 to 26 illustrates the effect of the Weissenberg number (We), on the primary shear stress i.e. axial skin friction (C_{fx}), secondary shear stress i.e. tangential skin friction (C_{gx}), wall couple stress (Wcs) and Nusselt number (Nux) distributions through the boundary layer regime. The Weissenberg number We is required to simulate the nonlinear relation between shear stress and strain rate in the non-Newtonian nanofluid. It characterizes the ratio of *elastic to viscous forces* in the magnetic polymer. It also expresses the ratio of *fluid relaxation time to specific time*. For large values of We, fluid relaxation time will greatly exceed the time scale of the flow and elastic stresses will be dominant. The reverse behavior will arise when relaxation time is exceeded by time scale of the flow for which the viscous effects will dominate, and elastic effects will subside. The magnetic polymer is therefore able to move with less tensile stress impedance when We is reduced, and this produces the observed acceleration in axial flow i.e. greater axial skin friction (C_{fx}) in Fig. 23.

It is interesting to note that the response to a change in Weissenberg number is delayed until larger values of the streamwise coordinate, ξ. This is linked to the delay in response of the spinning magnetic polymer and relaxation effects in the material. Similarly, an increment in tangential skin friction (C_{gx}) is also observed (Fig. 24) with increase in Weissenberg number We, again at larger values of the streamwise coordinate i.e. further from the cone vertex. However, values of tangential skin friction are always negative. Both axial and tangential boundary layer thicknesses are therefore reduced with stronger Weissenberg number. Viscoelastic effects vanish with We = 0. The magnetic polymer coating homogeneity and thickness consistency are in due course strongly influenced by the Weissenberg number, as emphasized in [24–26]. Viscoelasticity of the tangent hyperbolic model is characterized with polymer chain entanglement which produces a rod climbing effect, also known as Weissenberg effect, attributable to the imbalance in normal stresses. This entrains the magnetic polymer inwards and induces a climbing behaviour up the cone surface.

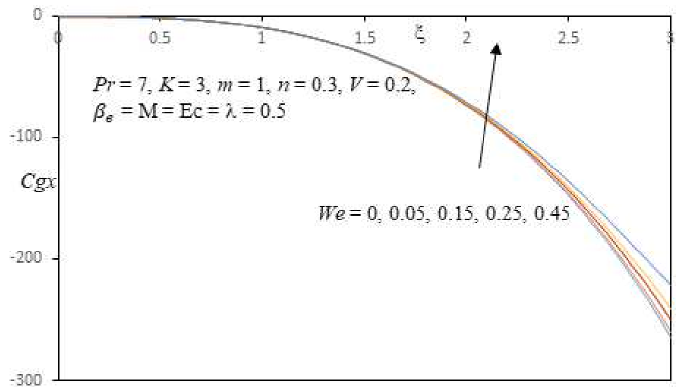

Fig. 24. Influence of We on secondary shear stress profiles.

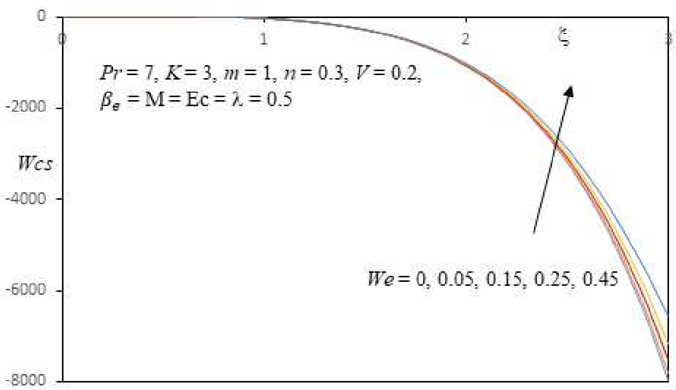

Fig. 25. Influence of We on wall couple stress profiles.

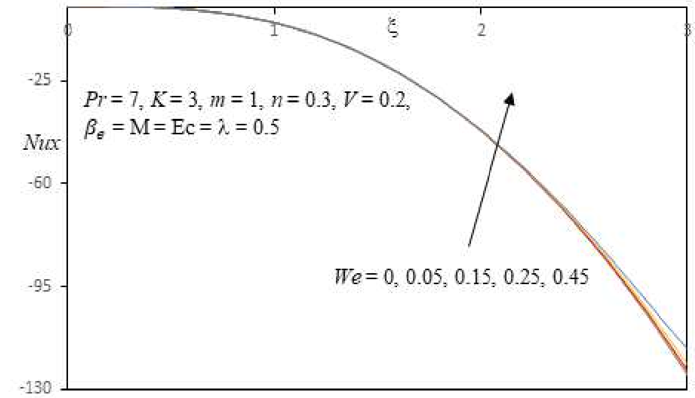

Fig. 26. Influence of *We* on Nusselt number profiles.

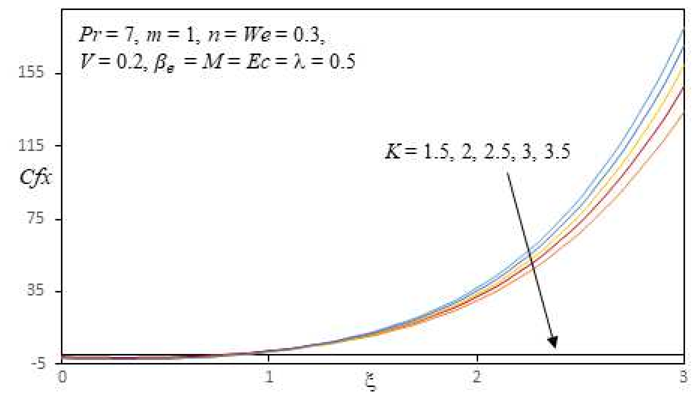

Fig. 27. Influence of *K* on primary shear stress profiles.

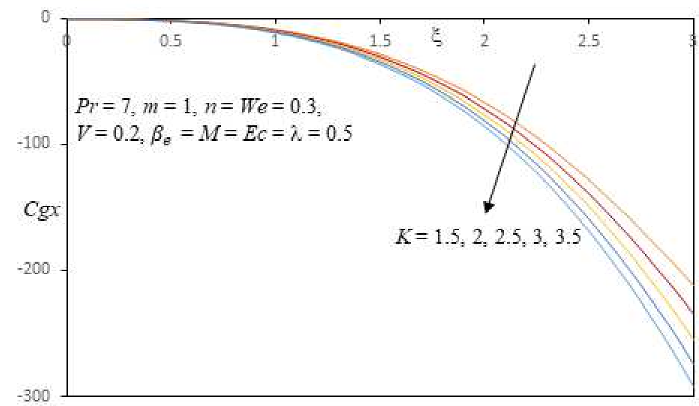

Fig. 28. Influence of *K* on secondary shear stress profiles.

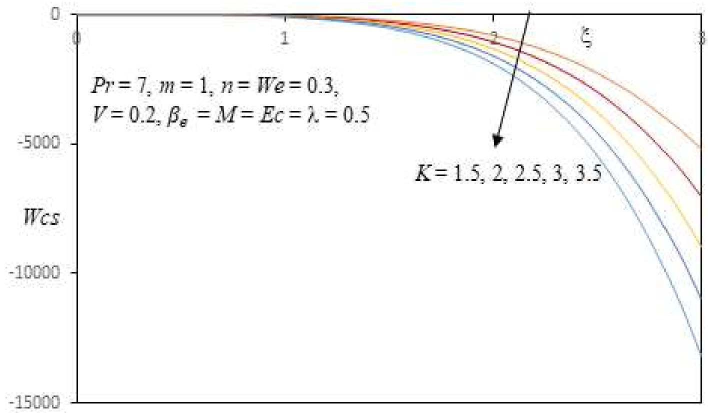

Fig. 29. Influence of *K* on wall couple stress profiles.

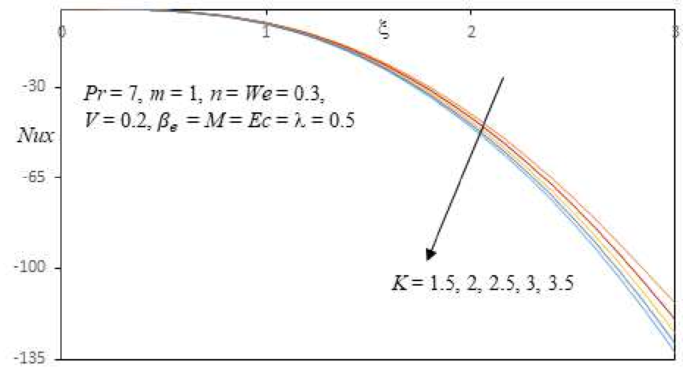

Fig. 30. Influence of K on Nusselt number profiles.

Figure 25 shows that the Eringen wall couple stress, which is also negative indicating reverse spin, is enhanced strongly with elevation in Weissenberg number. Increasing elasticity of the magnetic polymer, via the tangent hyperbolic model is conducive to encouraging stronger gyratory motions of the micro-elements. Again, only significant modifications arise at larger values of the streamwise coordinate i.e. the couple stress is invariant at smaller distance along the cone surface. Figure 26 indicates that Nusselt number is slightly enhanced at larger values of streamwise coordinate with a boost in Weissenberg number, *We*. Greater heat transfer is produced from the boundary layer to the cone surface (wall), with stronger viscoelasticity of the tangent hyperbolic model. This implies a cooling in the boundary layer which has also been confirmed with the temperature reduction observed in previous plots.

Figures 27 to 30 illustrates the effect of the Eringen vortex viscosity coupling parameter *K*, on the primary shear stress (axial skin friction) (C_{fx}), secondary shear stress (tangential skin friction) (C_{gx}), wall couple stress (*Wcs*) and Nusselt number (*Nux*) distributions through the boundary layer regime. A strong enhancement in normal skin friction component (Fig. 27) is induced with increasing Eringen coupling number (*K*), and this effect is amplified with larger values of streamwise coordinate (ξ). Tangential skin friction (Fig. 28) conversely is significantly damped with a hike in *K* values. A strong deceleration in the tangential flow is therefore associated with stronger micropolar vortex viscosity. According to Fig. 29, wall couple stress is also suppressed with increasing *K* values. Maximum deceleration is associated with the largest value of streamwise coordinate i.e. furthest from the cone vertex. Finally, Fig. 30 also shows that a substantial depreciation in Nusselt number is induced with increment in *K* values. Heat transfer to the cone surface (wall) is suppressed with stronger micropolarity. This is due to the net transfer of heat into the boundary layer which as shown earlier produces a strong heating effect and amplification in thermal boundary layer thickness.

Table 2 presents the influence of the tangent-hyperbolic rheological power law index (*n*), material parameter (*V*) on local skin frictions (C_{fx} and C_{gx}), wall couple stress (*Wcs*) and heat transfer rate (*Nu*), along with a variation in the stream wise coordinate values, ξ. An increase in tangent hyperbolic power law index suppresses the normal skin friction and Nusselt number but elevates the tangential skin friction and wall couple stress magnitudes. Increasing streamwise coordinate also produces an increase in normal skin friction but generates a depletion in tangential skin friction, wall couple stress and Nusselt number. Higher values of the micropolar gyro-viscosity material parameter $(V_1 = \nu / j\Omega\sin\varphi)$ induces a decrease in normal skin friction, tangential skin friction, wall couple stress but enhances the Nusselt number. With increment in streamwise coordinate, normal skin friction and wall couple stress are strongly elevated; tangential skin friction and Nusselt number are however very prominently suppressed with streamwise coordinate, ξ.

Table 3 lists the results for the influence of microinertia mass micropolar parameter (λ) and Prandtl number (*Pr*) on local skin frictions (C_{fx} and C_{gx}) wall couple stress (*Wcs*) and heat transfer rate (*Nu*), along with a variation in the streamwise coordinate (ξ). An increase in microinertia mass micropolar parameter $(\lambda = \gamma / j\mu)$ boosts and slightly increases tangential skin friction but strongly suppresses wall couple stress and Nusselt number magnitudes. Increasing streamwise coordinate boosts the normal skin friction but very markedly reduces tangential skin friction, wall couple stress and Nusselt number. An elevation in Prandtl number is observed to enhance axial skin friction but depletes the tangential skin friction, wall couple stress and Nusselt number. The larger values of Prandtl number (> 1), correspond to lower thermal conductivity of the magnetic polymer. This suppresses heat transfer to the cone surface and therefore Nusselt number is reduced. The relative contribution of thermal convection to thermal conduction at the cone surface is also therefore diminished *i.e.* the cone surface is cooled. With progressive increase in streamwise coordinate, the axial skin friction is clearly elevated whereas the tangential skin friction, wall couple stress and Nusselt number are all suppressed. A strong cooling is therefore produced also with distance from the cone vertex along the slant periphery.

Table 2. Values of C_{fx}, C_{gx}, Wcs and *Nu* for different of *n*, V and ξ.

n	V	ξ = 1.0				ξ = 2.0				ξ = 3.0			
		C_{fx}	C_{gx}	Wcs	*Nu*	C_{fx}	C_{gx}	Wcs	*Nu*	C_{fx}	C_{gx}	Wcs	*Nu*
0		2.9511	-11.398	-37.07	-5.7388	39.7702	-88.308	-1013.8	-46.393	194.269	-317.06	-7583.2	-137.72
0.1		2.7482	-10.762	-39.474	-5.5252	37.3901	-83.286	-1028.4	-44.946	180.934	-293.69	-7498.3	-133.19
0.2	0.2	2.5230	-10.102	-42.025	-5.2919	34.8565	-77.881	-1041	-43.327	166.050	-267.14	-7330.6	-127.65
0.3		2.2724	-9.4123	-44.717	-5.0341	32.1265	-71.976	-1049.5	-41.476	148.048	-235.34	-7000.2	-119.84
0.4		1.9919	-8.6816	-47.532	-4.7449	29.1222	-65.379	-1049.5	-39.289	110.371	-154.99	-5372.5	-102.59
	0	2.2305	-9.3290	7.6232	-5.1875	32.5953	-71.372	15.636	-42.376	151.617	-233.88	26.443	-121.74
	0.2	2.2724	-9.4123	-44.717	-5.0341	32.1265	-71.976	-1049	-41.476	148.048	-235.34	-7000.2	-119.84
0.3	0.4	2.2339	-9.4512	-91.282	-4.9659	31.5332	-72.281	-1911	-41.044	144.815	-236.11	-1260.3	-118.88
	1	2.1537	-9.5149	-200.33	-4.8588	30.5414	-72.790	-3856	-40.366	139.55	-237.39	-24793	-117.36
	2	2.0798	-9.5672	-335.73	-4.7748	29.7706	-73.211	-6205	-39.845	135.622	-238.44	-39131	-116.18

Table 3. Values of C_{fx}, C_{gx}, Wcs and Nu for different of λ, Pr and ξ.

λ	Pr	ξ = 1.0				ξ = 2.0				ξ = 3.0			
		C_{fx}	C_{gx}	Wcs	Nu	C_{fx}	C_{gx}	Wcs	Nu	C_{fx}	C_{gx}	Wcs	Nu
0.05		2.1435	-9.523	-.321.80	-4.8440	30.4009	-72.919	-6035.8	-40.233	139.3577	-237.67	-37942	-117.13
0.25		2.2454	-9.440	-88.416	-4.9835	31.6579	-72.215	-1872.9	-41.134	145.5807	-235.93	-12261	-119.09
0.5	7	2.2724	-9.412	-44.717	-5.0341	32.1265	-71.976	-1049.5	-41.476	148.0479	-235.34	-7000	-119.84
0.75		2.2798	-9.398	-23.340	-5.0599	32.3470	-71.864	-728.6	-41.684	149.2564	-235.07	-4917	-120.20
1		2.2809	-9.389	-19.771	-5.0766	32.4746	-71.796	-555.2	-41.746	149.9808	-234.90	-3781	-120.42
	0.5	0.6398	-1.422	0.2063	0.3015	5.0835	-10.534	-2.5765	-0.3912	21.2422	-33.97	-19.788	-2.1100
	1	0.9105	-2.762	0.0606	-0.0126	9.3885	-20.748	-22.346	-3.3873	39.5749	-67.15	-153.34	-10.991
0.5	3	1.1824	-4.088	-1.5456	-0.6054	13.8054	-30.937	-78.054	-8.1425	59.5064	-100.51	-523.12	-24.726
	5	1.7273	-6.750	-13.569	-2.4272	22.8691	-51.437	-371.90	-22.133	102.4455	-167.78	-2495	-64.782
	7	2.2724	-9.412	-44.717	-5.0341	32.1265	-71.976	-1049.5	-41.476	148.0479	-235.34	-7000	-119.84
	10	3.0901	-13.405	-146.66	-10.244	46.2626	-102.83	-3116.1	-79.464	219.8802	-336.99	-20892	-227.61

7. Conclusions

As a simulation of electroconductive polymer (ECP) spin coating processes, in this article, a mathematical model has been developed for evaluating the composite effects of Hall current and Ohmic (Joule) heating on laminar convection swirling boundary layer flow and heat transfer in tangent hyperbolic *micropolar fluid* external to a non-isothermal spinning cone. The transformed 9th order, coupled, nonlinear multi-degree ordinary differential coating boundary layer flow problem has been solved computationally using the implicit Keller box finite difference method (KBFDM). Validation of the MATLAB-based code has been included for the special case where tangent hyperbolic shear-thinning rheology is negated (zero power-law index and vanishing Weissenberg number). A detailed study of the impact of key control parameters, on tangential and axial velocities, angular velocity (micro-rotation), temperature, skin friction components, wall couple stress and Nusselt number have also been presented. The computations have shown that:

(i) An increment in Weissenberg number (*We*) produces a weak enhancement in axial skin friction, tangential skin friction, wall couple stress and local Nusselt number with large distance from the cone vertex (*i.e.* $\xi-$ coordinate).

(ii) An increase in Eringen micropolar coupling parameter, *K* strongly accentuates the axial skin friction whereas it damps the tangential skin friction, wall couple stress and local Nusselt number with progression in $\xi-$ coordinate.

(iii) Micro-rotation (angular) velocity exhibits an oscillatory response to increment in hyperbolic power-law index (*n*) with a reverse spin near the cone surface and a peak spin at maximum value of *n* further from it. Temperature is consistently damped throughout the boundary layer transverse to the cone surface with a rise in *n*.

(iv) Increasing magnetic interaction parameter (*M*) accelerates the axial velocity, damps the tangential velocity and micro-rotation (near the wall) and elevates temperatures strongly.

(v) Increasing Eckert number (*Ec*) enhances temperature and accelerates the axial flow and damps the tangential flow and also the angular velocity (micro-rotation) near the wall.

(vi) An increment in Hall parameter (β_e) produces significant cross flow and damps the axial velocity but elevates the tangential flow and temperature (and thermal boundary layer thickness) and enhances angular velocity further from the cone surface.

The present investigation aimed to reveal some intricate fluid dynamic characteristics associated with swirl coating of rotating conical substrates with magneto-rheological polymers. Attention has however been confined to momentum and heat transfer. Future investigations may address *wall slip effects* [71] and also *mass transfer* and explore non-Fickian diffusion [72] involving solute relaxation. Efforts in these directions are underway and will be communicated imminently.

Author Contributions

S. Abdul Gaffar performed the study conception, design, material preparation, data collection and analysis. O. Anwar Bég, T.A. Bég, S. Kuharat and P. Ramesh Reddy wrote the first draft of the manuscript. The manuscript was written through the contribution of all authors. All authors discussed the results, reviewed, and approved the final version of the manuscript.

Acknowledgments

We are expressing our deepest gratitude and appreciation for the assistance and support received throughout the completion of this research paper from my co-authors. I want to take this opportunity to acknowledge the contributions of the individuals who played a significant role in successfully completing this research project.

Conflict of Interest

The authors declared no potential conflicts of interest concerning the research, authorship, and publication of this article.

Funding

The authors received no financial support for the research, authorship, and publication of this article.

Data Availability Statements

The datasets generated and/or analysed during the current study are available from the corresponding author on reasonable request.

Nomenclature

B	Micropolar material parameter	V_1	material parameter
B_0	Constant imposed magnetic field	We	Weissenberg number
C_f	Skin friction coefficient	x	Stream wise coordinate
c_p	Specific heat	y	Transverse coordinate
e	Electron charge	**Greek**	
Ec	Eckert number	φ	Semi-vertex angle of the cone
f	Non-dimensional steam function	α	Thermal diffusivity
Gr_x	Local Grashof number	β	The coefficient of thermal expansion
g	Acceleration due to gravity	η	The dimensionless radial coordinate
k	Vortex viscosity	μ	Dynamic viscosity
K	Couple parameter	ν	Kinematic viscosity
j	Microinertia per unit mass	θ	Non-dimensional temperature
M	Magnetic parameter	ρ	Density of non-Newtonian fluid
m_e	Mass of electron	ξ	Dimensionless tangential coordinate
m	Surface temperature exponent	ψ	Dimensionless stream function
n	Power law index	γ	Spin gradient viscosity
N	Microrotation component	Γ	Time dependent material constant
n_e	Electron number density	Π	Second invariant strain tensor
Nu	Heat transfer rate (local Nusselt number)	Ω	Angular velocity
Pr	Prandtl number	β_e	Hall parameter ($\omega_e t_e$)
Re	Local Reynolds number	ω_e	Electron frequency (eB_0/m_e)
Ra	Local Rayleigh number	σ	Electrical conductivity ($e^2 n_e t_e/m_e$)
r	Local radius of the cone	λ	Gyro-viscosity micropolar material parameter
T	Temperature of the fluid	**Subscripts**	
t_e	Electron collision time	w	Conditions at the wall (cone surface)
u, v, w	Non-dimensional velocity components along the x, y, z directions, respectively	∞	Free stream conditions
V	Velocity vector		

References

[1] Danglad-Flores, J., Eickelmann, S., Riegler, H., Deposition of polymer films by spin casting: A quantitative analysis, *Chemical Engineering Science*, 179, 2018, 257–264.

[2] Kreith, F., Convection heat transfer in rotating systems, *Advances in Heat Transfer*, 5, 1968, 129-251.

[3] Bég, O.A., Kabir, N., Uddin, M.J., Ismail, A.I.M., AlginahI, Y., Numerical investigation of Von Karman swirling bioconvective nanofluid transport from a rotating disk in a porous medium with Stefan blowing and anisotropic slip effects, *Proc. IMechE - Part C- J. Mechanical Engineering Science*, 235 (19), 2021, 3933-3951.

[4] Panda, S.K., Chhabra, R.P., Laminar forced convection heat transfer from a rotating cylinder to power-law fluids, *Numerical Heat Transfer, Part A: Applications*, 59(4), 2011, 297-319.

[5] Weidner, D.E., Analysis of the flow of a thin liquid film on the surface of a rotating, curved, axisymmetric substrate, *Physics of Fluids*, 30(8), 2018, 082110.

[6] Kang, D., Nadim, A., Chugunova, M., Dynamics and equilibria of thin viscous coating films on a rotating sphere, *Journal of Fluid Mechanics*, 791, 2016, 495-518.

[7] Bég, O.A., Takhar, H.S., Nath, G., Chamkha, A.J., Mathematical modeling of hydromagnetic convection from a rotating sphere with impulsive motion and buoyancy effects, *Non-Linear Analysis: Modeling and Control*, 11, 3, 2006, 227-245.

[8] Anilkumar, D., Roy, S., Unsteady mixed convection flow on a rotating cone in a rotating fluid, *Applied Mathematics and Computation*, 155(2), 2004, 545–561.

[9] Ravindran, R., Roy, S., Momoniat, E., Effects of injection (suction) on a steady mixed convection boundary layer flow over a vertical cone, *International Journal of Numerical Methods for Heat and Fluid Flow*, 19(3/4), 2009, 432–444.

[10] Tien, C.L., Tsuji, I.J., A theoretical analysis of laminar forced flow and heat transfer about a rotating cone, *ASME Journal of Heat Transfer*, 87(2), 1965, 184–190.

[11] Afshar, A.F.S., Gabe, D.R., Sewell, Mass transfer at rotating cone electrodes, *Journal of Applied Electrochemistry*, 21, 1991, 32–39.

[12] Papanastasiou, T.C., Alexandrou, A.N., Graebel, W.P., Rotating thin films in bell sprayers and spin coating, *Journal of Rheology*, 32, 1988, 485–509.

[13] Zhang, L., Zhang, M., Zhang, X., Liu, Z., Modelling of ice accretion on rotating cone in aero-engine, *AIAA 2016-5059: Session: Gas Turbine Inlets, 52nd AIAA/SAE/ASEE Joint Propulsion Conference*, Salt Lake City, Utah, USA, July 25-27, 2016.

[14] Tambe, S., Schrijer, F., Veldhuis, L., Rao, A.G., Spiral instability modes on rotating cones in high-Reynolds number axial flow, *Physics of Fluids*, 34, 2022, 034109.

[15] Bég, O.A., Uddin, M.J., Bég, T., Gorla, R.R., Numerical simulation of self-similar thermal convection from a spinning cone in anisotropic porous medium, *Journal of Hydrodynamics Series B*, 28(2), 2016, 184-194.

[16] Turkyilmazoglu, M., The flow and heat in the conical region of a rotating cone and an expanding disk, *International Journal of Numerical Methods for Heat & Fluid Flow*, 33(6), 2023, 2181-2197.

[17] Turkyilmazoglu, M., A note on the induced flow and heat transfer due to a deforming cone rotating in a quiescent fluid, *Journal of Heat Transfer*, 140(12), 2018, 124502.

[18] Turkyilmazoglu, M., On the purely analytic computation of laminar boundary layer flow over a rotating cone, *International Journal of Engineering Science*, 47(9), 2009, 875-882.

[19] Flack, W.W., Soong, D.S., Bell, A.T., Hess, D.W., A mathematical model for spin coating of polymer resists, *Journal of Applied Physics*, 56(4), 1984, 1199-1206.

[20] Middleman, S., The effect of induced airflow on the spin coating of viscous liquids, *Journal of Applied Physics*, 62(6), 1987, 2530-2532.

[21] Hall, D.B., Underhill, P., Torkelson, J.M., Spin coating of thin and ultrathin polymer films, *Polymer Engineering & Science*, 38(12), 1998, 2039-2045.

[22] Martins, P., Lanceros-Méndez, S., Polymer-based magnetoelectric materials, *Advanced Functional Materials*, 23, 2013, 3371–3385.

[23] Solawu, S.O., Shamshuddin, M., Bég, O.A., Influence of magnetization, variable viscosity and thermal conductivity on Von Karman swirling flow of H2O-Fe3O4 and H2O-Mn-ZNFe2O4 ferromagnetic nanofluids from a stretchable rotating disk: smart spin coating simulation, *Materials Science and Engineering B*, 279, 2022, 115659.
[24] Martins, P., Lopes, A.C., Lanceros-Mendeza, S., Electroactive phases of poly (vinylidene fluoride): determination, processing and applications, *Progress in Polymer Science*, 39, 2014, 683–706.
[25] Yoon, J.S., Yoo, Y.E., Choi, D.S., A study on the fabrication of rounded patterns by spin coating of photoresist on silicon substrate with microstructures, *Polymer Engineering & Science*, 52(3), 2012, 499-506.
[26] Eringen, A.C., Theory of micropolar fluids, *Journal of Mathematics and Mechanics*, 16, 1966, 1-16.
[27] Eringen, A.C., Theory of thermomicrofluids, *Journal of Mathematical Analysis and Applications*, 38(2), 1972, 480-496.
[28] Gajjela, N., Jangili, S., Murthy, J.R.V., Bég, O.A., Mathematical modelling of entropy generation in magnetized micropolar flow between co-rotating cylinders with internal heat generation, *Alexandria Engineering Journal*, 55(3), 2016, 1969-1982.
[29] Gorla, R.S.R., Nakamura, S., Mixed convection of a micropolar fluid from a rotating cone, *International Journal of Heat and Fluid Flow*, 16(1), 1995, 69-73.
[30] Ahmad, S., Ali, K., Bashir, H., Interaction of micropolar fluid structure with the porous media in the flow due to a rotating cone, *Alexandria Engineering Journal*, 60, 2021, 1249-1257.
[31] Shamshuddin, M.D., Bég, O.A., Sheri, S.R., Kadir, A., Rotating unsteady multi-physico-chemical magneto-micropolar transport in porous media: Galerkin finite element study, *Computational Thermal Sciences*, 10(2), 2018, 167–197.
[32] Hina, S., Roman, U., Inam, S., Kanwal, S., Bilal, M., A numerical study of rotating Bödewadt flow of micropolar fluid over porous disk, *Proc IMechE Part E: J Process Mechanical Engineering*, 236(5), 2022, 2147–2154.
[33] Shelukhina, V.V., Neverov, V.V., Thermodynamics of micropolar Bingham fluids, *Journal of Non-Newtonian Fluid Mechanics*, 236, 2016, 83-90.
[34] Prasad, V.R., Gaffar, S.A., Bég, O.A., Heat and mass transfer of a nanofluid from a horizontal cylinder to a micropolar fluid, *AIAA Journal of Thermophysics Heat Transfer*, 29(1), 2015, 127-139.
[35] Afzal, S., Siddique, I., Jarad, F., Ali, R., Abdal, S., Hussain, S., Significance of double diffusion form unsteady Carreau micropolar nanofluid transportation across an extending sheet with thermo-radiation and uniform heat source, *Case Studies in Thermal Engineering*, 28, 2021, 101397.
[36] Gaffar, S.A., Bég, O.A., Prasad, V.R., Khan, B.M.H., Kadir, A., Computation of Eyring-Powell micropolar convective boundary layer flow from an inverted non-isothermal cone: thermal polymer coating simulation, *Computational Thermal Sciences*, 12(4), 2020, 329–344.
[37] Khan, M.N., Khan, A.A., Wang, Z., Alrihieli, H.F., Eldin, S.M., Aldosari, F.M., Elseesy, I.E., Flow investigation of the stagnation point flow of micropolar viscoelastic fluid with modified Fourier and Fick's law, *Scientific Reports*, 13, 2023, 9491.
[38] Gaffar, S.A., Bég, O.A., Prasad, V.R., Mathematical modelling of natural convection in a third-grade viscoelastic micropolar fluid from an isothermal inverted cone, *Iranian Journal of Science and Technology, Transactions of Mechanical Engineering*, 44, 2020, 383–402.
[39] Habib, U., Abdal, S., Siddique, I., Ali, R., A comparative study on micropolar, Williamson, Maxwell nanofluids flow due to a stretching surface in the presence of bioconvection, double diffusion and activation energy, *International Communications in Heat and Mass Transfer*, 127, 2021, 105551.
[40] Basha, H.T., Sivaraj, R., Prasad, V.R., Beg, O.A., Entropy generation of tangent hyperbolic nanofluid flow over a circular cylinder in the presence of nonlinear Boussinesq approximation: a non-similar solution, *Journal of Thermal Analysis and Calorimetry*, 143, 2021, 2273–2289.
[41] Gaffar, S.A., Prasad, V.R., Reddy, S.K., Bég, O.A., Magnetohydrodynamic free convection boundary layer flow of non-Newtonian tangent hyperbolic fluid from a vertical permeable cone with variable surface temperature, *Journal of the Brazilian Society of Mechanical Sciences and Engineering*, 39, 2017, 101–116.
[42] Malik, M.Y., Salahuddin, T., Hussain, A., Bilal, S., MHD flow of tangent hyperbolic fluid over a stretching cylinder: Using Keller box method, *Journal of Magnetism and Magnetic Materials*, 395, 2015, 271-276.
[43] Prakash, J., Tripathi, D., Akkurt, N., Bég, O.A., Tangent hyperbolic non-newtonian radiative bioconvection nanofluid flow from a bi-directional stretching surface with electro-magneto-hydrodynamic, Joule heating and modified diffusion effects, *European Physical Journal Plus*, 137, 2022, 472.
[44] Nasir, M., Waqas, M., Bég, O.A., Zamri, M., Leonard, H.J., Guedri, K., Dynamics of tangent-hyperbolic nanoliquids configured by stratified extending surface: Effects of transpiration, Robin conditions and dual stratifications, *International Communications in Heat and Mass Transfer*, 139, 2022, 106372.
[45] Asogwa, K.K., Goud, B.S., Shah, N.A., Yook, S.J., Rheology of electromagnetohydrodynamic tangent hyperbolic nanofluid over a stretching Riga surface featuring Dufour effect and activation energy, *Scientific Reports*, 12, 2022, 14602.
[46] Usman, Khan, W., Badruddin, I.A., Ghaffari, A., Ali, H.M., Heat transfer in steady slip flow of tangent hyperbolic fluid over the lubricated surface of a stretchable rotatory disk, *Case Studies in Thermal Engineering*, 24, 2021, 100825.
[47] Reddy, P.R., Gaffar, S.A., Khan, B.M.H., Venkatadri, K., Bég, O.A., Mixed convection flows of tangent hyperbolic fluid past an isothermal wedge with entropy: A mathematical study, *Heat Transfer*, 50, 2021, 2895-2928.
[48] Hughes, W.F., Young, F.J., *The Electro-magneto-dynamics of Fluids*, John Wiley, USA, 1966.
[49] Lee, S-J., Park, J-H., Choi, E-J., Jeong, Y.G., Microstructure and electrothermal properties of carbon films derived from a sustainable organically soluble wholly aromatic polyamide, *Diamond and Related Materials*, 136, 2023, 109980.
[50] Haque, A.B.M.T., Tutika, R., Gao, M., Martinez, A., Mills, J., Clement, J.A., Gao, J., Tabrizi, M., Shankar, M.R., Pei, Q., Bartlett, M.D., Conductive liquid metal elastomer thin films with multifunctional electro-mechanical properties, *Multifunctional Materials*, 3, 2020, 044001.
[51] Shamshuddin, M.D., Mishra, S.R., Bég, O.A., Kadir, A., Unsteady reactive magnetic radiative micropolar flow, heat and mass transfer from an inclined plate with Joule heating: a model for magnetic polymer processing, *Proc. IMechE- Part C – Journal of Mechanical Engineering Science*, 223(4), 2019, 1-8.
[52] Bég, O.A., Bég, T.A., Ferdows, M., Vasu, B., Kadir, A., Leonard, H.J., Kuharat, S., Unsteady nonlinear magnetohydrodynamic micropolar transport phenomena with Hall and ion-slip current effects: numerical study, *International Journal of Applied Electromagnetics and Mechanics*, 65, 2021, 371-403.
[53] Chandrawat, R.K., Joshi, V., Bég, O.A., Ion slip and Hall effects on generalized time-dependent hydromagnetic Couette flow of immiscible micropolar and dusty micropolar fluids with heat transfer and dissipation: a numerical study, *Journal of Nanofluids*, 10, 2021, 431–446.
[54] Turkyilmazoglu, M., Heat and Mass Transfer on the MHD Fluid Flow Due to a Porous Rotating Disk with Hall Current and Variable Properties, *Journal of Heat Transfer*, 133(2), 2011, 021701.
[55] Abo-Eldahab, E.M., Elaziz, M.A., Hall current and ohmic heating effects on mixed convection boundary layer flow of a micropolar fluid from a rotating cone with power-law variation in surface temperature, *International Communications in Heat and Mass Transfer*, 31(5), 2004, 751–762.
[56] Dinarvand, S., Saber, M., Abulhasansari, M., Micropolar fluid flow and heat transfer about a spinning cone with Hall current and Ohmic heating, *Proc IMechE Part C- Journal of Mechanical Engineering Science*, 228(11), 2014, 1900–1912.
[57] Keller, H.B., Numerical methods in boundary-layer theory, *Annual Review of Fluid Mechanics*, 10, 1978, 417-433.
[58] Bég, O.A., *Numerical methods for multi-physical magnetohydrodynamics*, Chapter 1, pp. 1-112, New Developments in Hydrodynamics Research, Nova Science, New York, 2012.
[59] Prasad, V.R., Gaffar, S.A., Reddy, E.K., Bég, O.A., Numerical study of non-Newtonian boundary layer flow of Jeffreys fluid past a vertical porous plate in a non-Darcy porous medium, *International Journal for Computational Methods in Engineering Science and Mechanics*, 15(4), 2014, 372-389.
[60] Al-Mdallal, Q., Prasad, V.R., Basha, H.T., Sarris, I., Akkurt, N., Keller box simulation of magnetic pseudoplastic nano-polymer coating flow over a circular cylinder with entropy optimisation, *Computers & Mathematics with Applications*, 118, 2022, 132-158.
[61] Kamran, A., Azhar, E., Numerical outlook of a viscoelastic nanofluid in an inclined channel via Keller box method, *International Communications in Heat and Mass Transfer*, 137, 2022, 106260.
[62] Shi, Q.H., Shabbir, T., Mushtaq, M., et al., Modelling and numerical computation for flow of micropolar fluid towards an exponential curved surface: a Keller box method, *Scientific Reports*, 11, 2021, 16351.
[63] Gaffar, S.A., Prasad, V.R., Vijaya, B., Bég, O.A., Mixed convection flow of magnetic viscoelastic polymer from a non-isothermal wedge with Biot number effects, *International Journal of Engineering Mathematics*, 2015(1), 2015, 287623.
[64] Gaffar, S.A., Prasad, V.R., Bég, O.A., Computational analysis of magnetohydrodynamic free convection flow and heat transfer of non-Newtonian tangent hyperbolic fluid from a horizontal circular cylinder with partial slip, *International Journal of Applied and Computational Mathematics*, 1, 2015, 651–675.
[65] Bég, O.A., Gaffar, S.A., Prasad, V.R., Uddin, M.J., Computational solutions for non-isothermal, nonlinear magnetoconvection in porous media with Hall/ionslip currents and Ohmic dissipation, *Engineering Science and Technology - an International Journal*, 19, 2016, 377-394.

[66] Willson, J., Boundary layers in micropolar liquids, *Mathematical Proceedings of the Cambridge Philosophical Society*, 67(2), 1970, 469-476.
[67] Gorla, R.S., Takhar, H.S., Boundary layer flow of micropolar fluid on rotating axisymmetric surfaces with a concentrated heat source, *Acta Mechanica*, 105, 1994, 1-10.
[68] Inudo, S., Miyake, M., Hirato, T., Electrical properties of CuI films prepared by spin coating, *Physica Status Solidi (A) Applications and Materials Science*, 210(11), 2013, 2395-2398.
[69] Hughes, W.F., Young, F.J., *The Electro-magneto-dynamics of Fluids*, John Wiley, USA, 1966.
[70] Bég, O.A., Zueco, J., Chang, T.B., Numerical analysis of hydromagnetic gravity-driven thin film micropolar flow along an inclined plane, *Chemical Engineering Communications*, 198(3), 2010, 312-331.
[71] Prasad, V.R., Rao, A.S., Reddy, N.B., Vasu, B., Bég, O.A., Modelling laminar transport phenomena in a Casson rheological fluid from a horizontal circular cylinder with partial slip, *Proc IMechE- Part E: Journal of Process Mechanical Engineering*, 227(4), 2013, 309-326.
[72] Nasir, M., Waqas, M., Bég, O.A., Zamri, N., Homotopy analysis of mixed convection flow of a magnetized viscoelastic nanofluid from a stretching surface in non-Darcy porous media with revised Fourier and Fickian approaches, *Waves in Random and Complex Media*, 1 – 28, 2023, doi: 10.1080/17455030.2023.2178824.

ORCID iD

Shaik Abdul Gaffar https://orcid.org/0000-0002-7368-1658
O. Anwar Bég https://orcid.org/0000-0003-0614-8711
S. Kuharat https://orcid.org/0009-0000-5739-9137
P. Ramesh Reddy https://orcid.org/0000-0002-6666-7444

How to cite this article: Abdul Gaffar S., et al., Analysis of External Magnetized Dissipative Thermo-convective Tangent Hyperbolic-micropolar Flow on a Rotating Non-isothermal Cone with Hall Current and Joule Dissipation: Electro-conductive Polymer Spin Coating, *J. Appl. Comput. Mech.*, 11(4), 2025, 1039-1059. https://doi.org/10.22055/jacm.2024.47703.4770